High Frequency Raster Magnets Design for the ARIEL Electron Target Station at TRIUMF

by

Mathew Ishida, P.Eng.
Bachelor of Engineering, British Columbia Institute of Technology, 2011

A Thesis Submitted in Partial Fulfilment of the Requirements
For the Degree of

MASTER OF APPLIED SCIENCE

In the Department of Electrical and Computer Engineering

Supervisory Committee

High Frequency Raster Magnets Design for the ARIEL
Electron Target Station at TRIUMF

By
Mathew Ishida, P.Eng.
Bachelor of Engineering, British Columbia Institute of Technology, 2011

Supervisory Committee

Dr. Jens Bornemann, Department of Electrical and Computer Engineering
Supervisor

Dr. Poman So, Department of Electrical and Computer Engineering
Departmental Member

Abstract

TRIUMF, Canada's nuclear and particle physics research laboratory is currently in development of an Advanced Rare Isotope Facility (ARIEL) that will contain a newly designed electron target station. The target at this station is susceptible to destruction from instantaneous spot heating of the beam. To mitigate this, a raster system consisting of two AC electromagnets was proposed. The two magnets will work in tandem, vertical and horizontal, bending to produce raster patterns at 10 kHz. Since complex patterns consist of harmonics higher than the fundamental frequency, a design frequency of 100 kHz was chosen. AC current causes eddy currents which lead to the skin effect, causing high frequency current to concentrate on the outside of the conductor. To address this, a conductor diameter smaller than the skin depth at the given frequency must be chosen. This led to the choice of litz wire consisting of 400 insulated strands for the conductor. The radiation resistance insulation ethylene tetrafluoroethylene (ETFE) was chosen for these conductors and a 3D printed polyethylene sulfide (PPS) will be used for the coil bobbins. The effects of eddy currents were eliminated from the core material by choosing ferrite, an amorphous material consisting of iron-oxide crystals. Simulations were completed to ensure a homogenous magnetic field in the region of the beam, and the subsequent pole profile was determined. Lastly, a metalized ceramic beampipe is used to integrate with the existing beamline and allow for discharge of any static buildup on the inner surface of the beampipe due to the electron beam.

Table of Contents

List of Tables

List of Figures

Acknowledgments

I have to first thank the entire staff at TRIUMF for allowing me the opportunity to further my education while working on this difficult solution. The many physicists, engineers, technicians and staff members who continually helped me to understand abstract concepts and answered all my questions earnestly, no matter how silly they were.

I would like to thank the University of Victoria for their support and help in completing this thesis during a pandemic, and my advisor, Dr. Jens Bornemann, for patiently answering my questions and diligently reviewing my work.

My boss, friend, and mentor Dr. Marco Marchetto has been an invaluable resource throughout this project. His ability to explain high level physics in a way that I can understand is uncanny. This project truly could not have been completed without his guidance.

Lastly, I want to thank the late Douglas Adams, for showing me there are no ends to imagination and what is possible, as long as you know where your towel is!

Dedication

I dedicate this thesis to my loving wife Yui and our two beautiful

kitties Yukimi & Daifuku. Without their love and support,

I may have given up.

Nomenclature

ARIEL – Advanced Rare IsotopE Laboratory

RS – Requirements Specification

MeV – Mega-electron Volt

UBC – University of British Columbia

SFU – Simon Fraser University

CERN – European Council for Nuclear Research

CRT – Cathode Ray Tube

Hi-Lumi – High Luminosity

AC – Alternating Current

DC – Direct Current

OFHC – Oxygen-Free High Thermal Conductivity

RS - Requirement Specification

T - Tesla

Tm – Tesla Meter

G – Gauss

μ_o – Permeability of free space ($4\pi \times 10^{-7}$ H/m)

UCN – Ultra Cold Neutron

B4N – Beamline Four North

EPICS – Experimental Physics and Industrial Control System

Chapter 1 - Introduction

The following sections outline a brief introduction to TRIUMF, the role of electromagnets in accelerator science and an overview of the subsequent project of this thesis.

1.1 Introduction to TRIUMF

TRIUMF, Canada's nuclear and particle physics research laboratory came to fruition from a collaborative vision, in 1965, between three universities, SFU, UBC and UVIC. Their goal: to create the world's largest cyclotron and study subatomic particles [1]. Since then, TRIUMF has grown to become a multinational collaborative science institute supported by fourteen universities across Canada.

Along with the largest Cyclotron, TRIUMF now houses an electron linear accelerator, three smaller commercial cyclotrons and a variety of experimentation laboratories. Along with its national projects, TRIUMF collaborates with labs all over the world, including the Hi-Lumi upgrade project for the large hadron collider at CERN.

The newest project is centred around increasing TRIUMF's scientific productivity by 2-3 times it's current level. This new Advanced Rare Isotope Laboratory (ARIEL) will have the capacity to create high intensity rare isotopes that are typically short-lived and only seen in the stars [2]. Along with advancements in medical treatment, these new isotopes will be studied to further understand the origins of our universe. This thesis project is a direct result of the development of this new facility.

1.2 Role of Electromagnets in Accelerator Science

Since Hans Christian Oersted's first demonstration of electromagnetism in the 1800's, physicists have been working with the close relationship between electricity and magnetism [3]. As electrons and protons are shot through vacuum tubes at velocities near the speed of light, electromagnets provide the ability to steer, shape and focus the particle beams. These magnets are created by applying an electrical current to a set of copper windings, which, in turn, creates a force that can be applied to the particle beams. Dipoles (Fig. 1), for example, use two separate coils with north and south poles facing each other [3], to steer beams left and right, or up and down. Quadrapoles (Fig. 1), on the other hand, contain four coils with their similar poles facing each other, and are used to focus, or defocus, the beams. Although there are many other forms of electromagnets, such as sextupoles, octupoles, kickers and septums, these are the two main types of electromagnets used in accelerators all over the world.

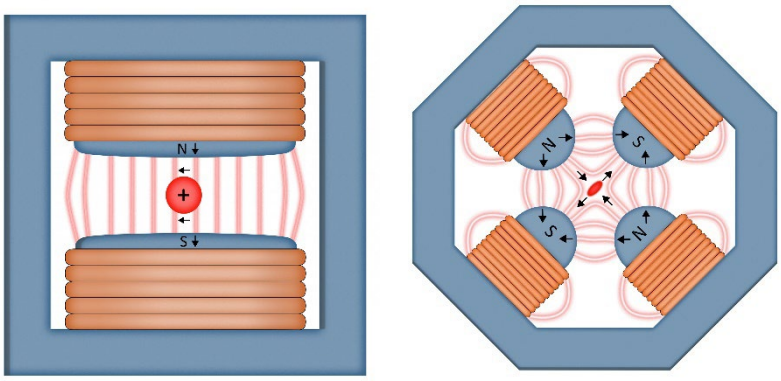

Figure 1 – Dipole (Left) & Quadrapole (Right) Electromagnets [3]

Typically, particles are meant to collide with a target at the end of their journey and create radioactive isotopes, or in the case of CERN, with each other. As these beams contain very high energies, to avoid destruction of targets by local heating, it can be necessary to quickly move the beam in a specified pattern. This is known as rastering and is most commonly seen

in old CRT televisions in which electrons are rastered to create an image. In order to raster particle beams, the magnets are required to react very quickly, which means, instead of a constant direct current (DC), used for most accelerator magnets, they must be operated with alternating current (AC) at high frequencies. The difficulties in electromagnet design owing to these additional requirements are a fundamental topic of this thesis.

1.3 Rastering at Other Labs

As rastering is not a new concept in accelerator science, it is important to understand processes applied at other labs around the world. The following outlines three examples of this.

1.3.1 Lawrence Berkley Laboratory, California, USA [4]

Berkley labs has been using a raster system since the late 1980's for experimental patient therapy. Their need for rastering stems from the small diameter proton beams they produce, at 2.5 cm, with the desire to cover a larger target area of 40cm by 40 cm. With a maximum beam rigidity[1] of 8 T-m, this system has been designed using two AC magnets in tandem. Initially, a fast-scanning magnet, at 40 Hz, 6 m from the target, scans in one plane, while the other, 4.7 m from the target scans at 0.5 Hz in the opposite plane.

To achieve a uniform magnetic field across the aperture width, the designers chose 160-turn bedstead coils wound with hollow-copper conductors; 0.647 cm square with a 0.315 cm diameter hole to allow for active cooling.

The electromagnet cores were manufactured from stainless steel laminated sheets smaller than the skin depth[2] at the specified operating frequencies; 1.5 mm thick for 40 Hz and 23.9 mm

[1] Beam rigidity is discussed in Chapter 2.3
[2] Skin depth and its effects are discussed in Chapter 3.3

thick for the 0.5 Hz magnet. The laminations were then compressed together using three hydraulic jacks and held firm by use of permanent compression bars pinned to the cores.

A long magnet length of 1m was selected to lower the effects of eddy currents[3], ramp rates, and the overall field requirements. Fig. 2 shows a monochromatic image of the fast-scanning magnet with a schematic of their raster system.

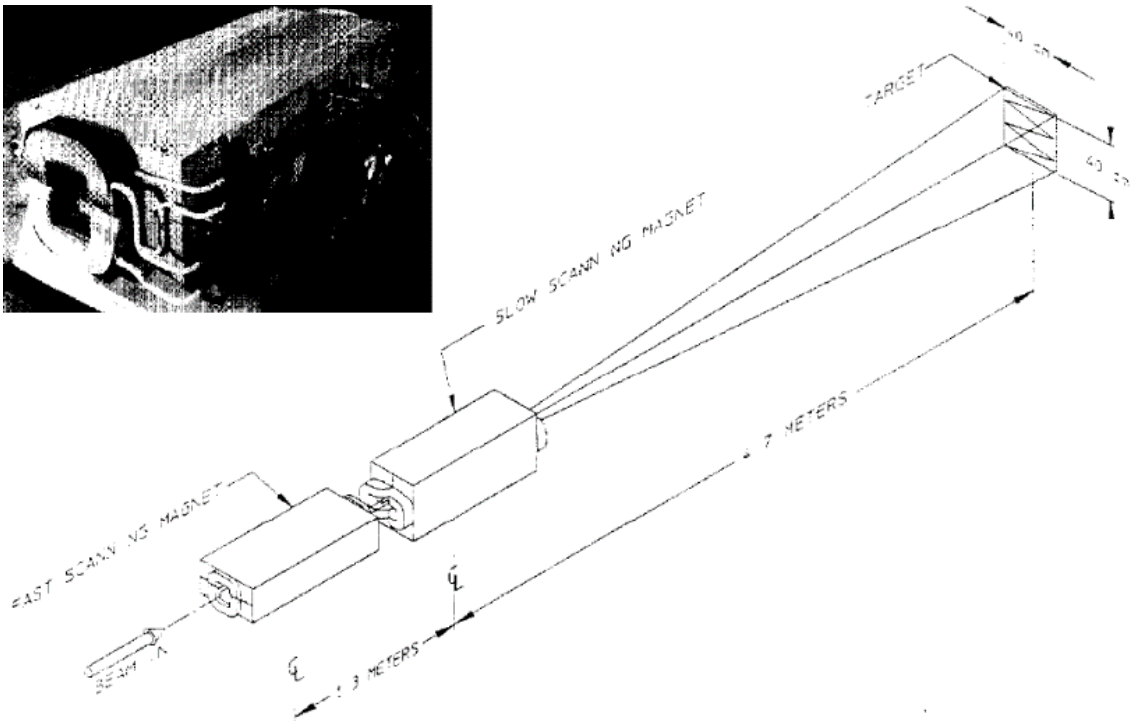

Figure 2 - Berkley Labs Raster System Schematic and Magnet Image (scanned from 1987 conference papers) [4]

As one of the older raster systems in operation and with the relatively low frequency of 40 Hz it is interesting to note how the design follows technologies that existed at the time, such as the CRT television and thin stainless-steel plates. The preceding examples, employ newer conductors and composites to achieve much higher frequencies.

[3] Eddy currents are discussed in Chapter 3.4

1.3.2 Thomas Jefferson National Accelerator Facility, Virginia, USA [5] [7]

At the Jefferson facility, fast rastering has been used for their cryogenic target experiments since 1996, with a new linear raster system that began operation in 2002. Their newest raster system, operating with two magnets in tandem, was based on eliminating beam heating effects on targets allowing for the higher currents that are often requested by experimenters. This was done by focussing on two points during design, to create the highest linear velocity and to suppress the turning time as much as possible. Through mathematical simulations, the fundamental frequency of rastering was determined to be 25 kHz, and with consideration for the first three harmonics[4], a design frequency of 75 kHz was chosen. At this target location, their electron beam energy ranges from 0.8-12 GeV, requiring a maximum central field of 341 G (0.0314 T) at 100 A, with a maximum overall field integral of 8100 G-cm (0.0081 T-m).

With their high frequency requirements, a special type of copper conductor know as litz[5] wire was used for the magnet coils. Each magnet consists of two bedstead coils with 12 turns each, using litz wire containing 1650 strands of AWG 38. This results in a current density of 1.0 A/mm^2, an inductance of 88 μH and a DC resistance of 0.04 Ω. Bedstead coils were chosen due to fitment with beam pipes and their moderate uniform field volume.

To mitigate the high frequency effects due to eddy currents and associated power losses, Jefferson lab chose to omit magnet cores, effectively making these air-core magnets. This allows the response between the excitation current and the induced magnetic field to be spontaneous, and field information to be obtained by either a pickup coil or a sensor on the driving current. Without a core to contain the magnetic field, fringe fields are a concern but by

[4] Fundamental frequencies are discussed in Chapter 2.5
[5] Litz wire is discussed in Chapter 3.4

using the sharp cut-off fringing field (SCOFF) approximation, which neglects the effects of fields outside the magnets, designers were able to adjust the magnet effective length to compensate. The entire system is installed on G10 (a non-metallic material) girders about 20m from the target with no optics or focussing elements in-between. Fig. 3 shows a schematic of the Hall C beamline including the two raster magnets.

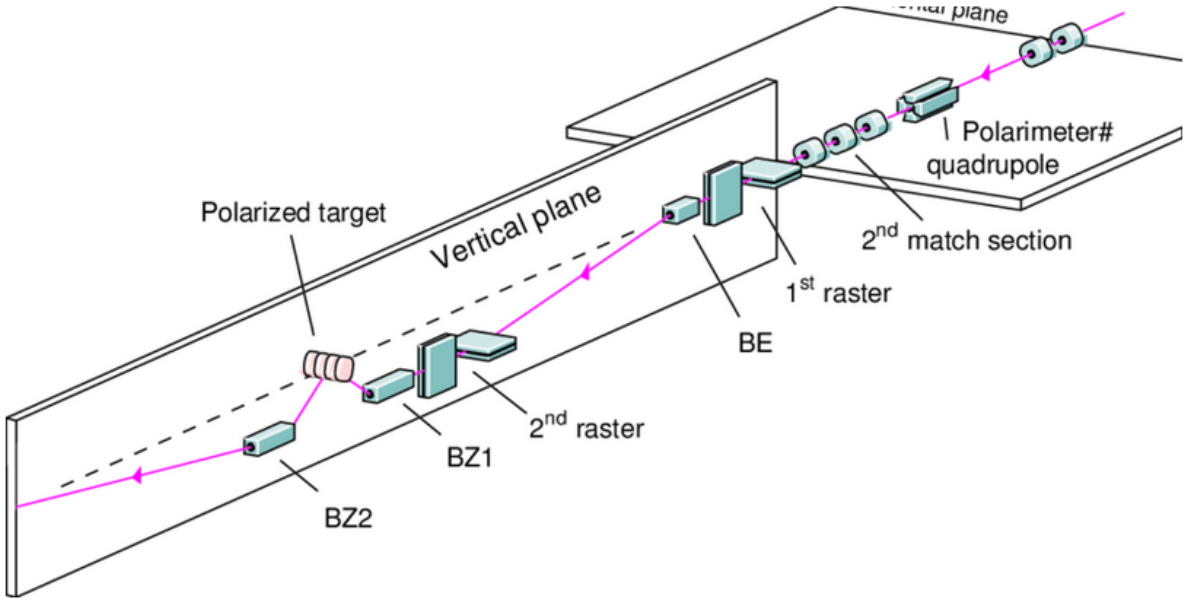

Figure 3 - Hall C Beam Line Chicane Magnets and Raster System [7]
(BE, BZ1 & BZ2 represent virtical dipole bending magnets)

Controlled using a custom power supply system, this linear raster system continues to be successfully operational at the Thomas Jefferson Accelerator Facility.

1.3.3 European Spallation Source, Lund, Sweden [6]

Although the new European Spallation Source (ESS) is still under construction and has not yet implemented their fast raster system, it has been developed under similar constraints seen in the ARIEL facility and has been an integral reference for this project. It is important to note that the raster system at the ESS will be used for proton beams, as opposed to the ARIEL facility which will raster electrons. Since protons are much heavier than electrons, approximately 2000 times [8], the energy required to raster and subsequent magnetic field requirements are quite different.

The proposed system for the ESS includes a total of 8 colinear raster scanning magnets (RSMs), two sets of four synchronized dipoles. Fig. 4 shows a schematic of one set of RSMs.

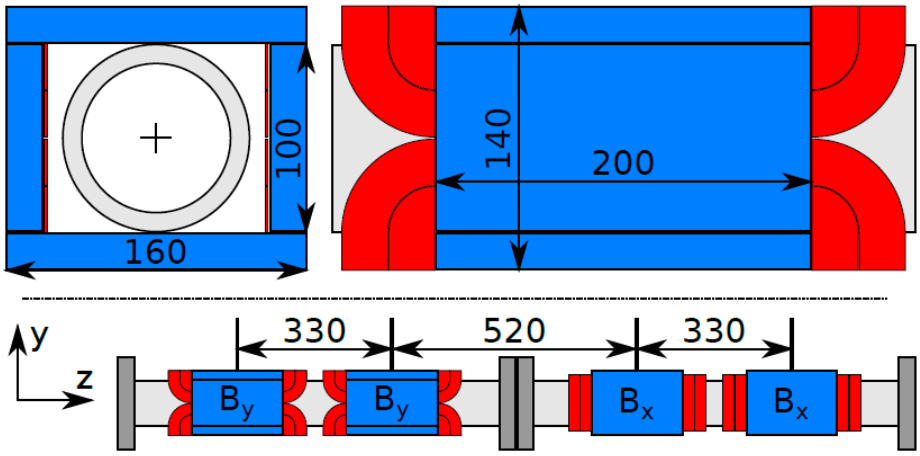

Figure 4 - ESS Raster Magnet System Schematic (dimensions in mm) [6]

The magnets are based on a window frame core which provides good field uniformity in the magnet aperture. With a beam rigidity of 9.29 T-m and a fundamental operating frequency of 40 kHz, the coils cannot be manufactured from typical conductors. The waveform chosen for this system is triangle and thus the higher harmonics are also considered. In this case, with a

skin depth in copper of 0.3 mm, the designers have chosen to cut from 1mm thick OFHC Cu plates and bend them into 2-turn bedstead coils.

With the high frequency requirements, it is again necessary to mitigate the effects of eddy currents and the ESS design team has done this by choosing NiZn ferrite as the core material. Ferrite is a ceramic like composite material that contains small particles of iron-oxide and allows for very high frequency response. It is often used in high voltage transformers[6]. Specifically, CMD5005 from Ceramic Magnetics, was suggested. This is ideal compared to the previous example at Jefferson Lab as the magnetic field can be contained within the ferrite core and fringe fields can be neglected.

The overall length of each magnet is to be 300 mm with an aperture diameter of 100 mm to fit the beampipe. Effects of eddy currents will also become an issue with metallic beampipes, as such, the beampipes for this system will be manufactured from a ceramic material. This brings other issues with build-up of induced charges on the ceramic and potential heating of the ferrite core. Typically, this would be mitigated by adding a very thin, 1μm, Ti metallization layer to the inner side of the tube[7], but after consulting with industry experts, the designers chose to forgo the coating in the initial design. Their justification is due to the high-energy rigid beam supplied by the ESS accelerator.

Supported by non-metallic materials, the raster system will also use a custom power system and is expected to be operational by 2025 with the completion of construction.

[6] Ferrite is further discussed in Chapter 3.5
[7] Beampipe metallization, and associated topic are discussed in Chapter 3.6

1.4 Overview of Thesis Project and Scope

ARIEL will contain a new electron target station that will utilize a new proton-to-neutron converter. This converter is very susceptible to localized heating from the high-powered electron beams and thus, the beam must be rastered at a minimum frequency of 10 kHz to avoid destruction. To accomplish this, two identical AC electromagnets will be developed, one to raster in the horizontal plane, and a second to raster in the vertical plane. These magnets will work in tandem to apply virtually any raster pattern desired onto the target converter.

The scope of this project includes the complete design of two identical alternating current electromagnets with 3D parametric modelling done in SolidWorks and magnet simulations completed in OPERA 3D. The vacuum beampipe, with integration into the existing beamline, is also included.

Omitted from the scope of this thesis is the power supply and control system as it will be a new customized system currently in development at TRIUMF. A set of specifications for the power system, including, voltage, current and inductance will be supplied based on calculated and simulated results.

1.5 Contributions

This project aims to contribute to the world of accelerator magnets by creating a system that rasters electrons at a high frequency utilizing the advancement in conductor and core technologies.

Chapter 2 - Requirements

The following outlines the requirements pertaining to the raster system for the ARIEL Electron Target East beamline at TRIUMF Inc. These requirements were compiled from released TRIUMF Document-143014, *ARIEL Electron Driver Beam and Diagnostic Requirements* [9].

2.1 Top Level Requirements

RS 2.1.1 Components of the raster system shall be compatible with 2.31×10^5 Gy of radiation.

Rationale: To survive the service lifetime of 30 years.

2.2 Location

RS 2.2.1 The raster system shall be located at a minimum of 5.2 m from the target.

Rationale: To accommodate the distance required for shielding between the last magnetic element and the target.

RS 2.2.2 The raster system shall integrate with the current beam line design.

Rationale: Beamline and associated components have been completed.

2.3 Beam Parameters

RS 2.3.1 The raster system shall be compatible with a 75 MeV electron beam.

Rationale: The ARIEL eLINAC will be capable of delivering a 75 MeV electron beam.

RS 2.3.2 The raster system shall be compatible with a beam size of 25 mm diameter.

Rationale: To accommodate full beam size at maximum power.

2.4 Rastering

RS 2.4.1 The largest scanned area shall be circular with 100 mm diameter.

Rationale: This is the area that may be required for an electron beam power of 100 kW.

RS 2.4.2 The smallest scanned area with homogeneous surface power deposition (spot scanning pixel size) shall be circular with 4 mm diameter.

Rationale: For very short-lived radioisotopes smaller targets may be used. A 4 mm irradiation spot size is appropriate for a 20 mm cylindrical target.

RS 2.4.3 Beam rastering shall be independent for horizontal and vertical planes.

Rationale: Two separate dipoles will be used.[8]

RS 2.4.4 The raster system shall be compatible with a raster frequency of 10 kHz.

Rationale: To avoid damaging the target with instantaneous heating.

RS 2.4.5 It should be possible to irradiate any shape within the minimum and maximum area defined above. It shall be possible to irradiate any circular, elliptical, and rectangular area within the minimum and maximum area defined above

Rationale: The target geometry is subject to constant improvements and may change once ARIEL is operational.

[8] Although it is possible for the further magnet to be slightly smaller, identical magnets will be used to minimize manufacturing cost and allow for interchangeability of components between magnets.

2.5 Design Frequency

The desired rastering frequency as set by *RS 2.4.4* is 10 kHz with *RS 2.4.5* requiring that any shape be possible within the minimum and maximum rastering areas. This is not practical as complex shapes require waveforms containing higher harmonics and thus higher frequencies than 10 kHz. In harmonic analysis, Fourier series are used as a way to represent periodic functions as infinite sums of sines and cosines [10], with the first term in the series being the fundamental frequency, in this case 10 kHz, and each additional term, or harmonic, a multiple of the first.

To quantify this open-ended frequency requirement, several potential raster patterns and their corresponding waveforms were investigated. Three examples of these are discussed in the following section. A design frequency of 100 kHz was then decided upon to allow for a maximum of 9 harmonics above the fundamental frequency of 10 kHz.

2.5.1 Raster Patterns and Waveforms

2.5.1.1 Ellipse – Pure Sine/Cosine Waveform

Figure 5 depicts an elliptical raster pattern within the maximum allowable diameter of 100 mm. This pattern is created by simultaneously supplying a pure sine wave to the vertical bender and a pure cosine to the horizontal. Figure 6 shows the corresponding waveforms to create the ellipse at 10 kHz. There are no additional frequency requirements to produce an ellipse, or any shape comprised of only a single harmonic.

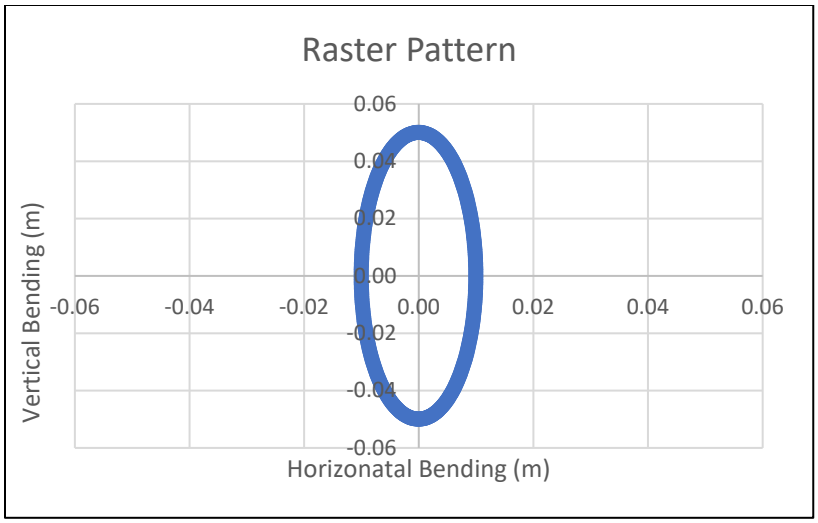

Figure 5 - Elliptical Raster Pattern

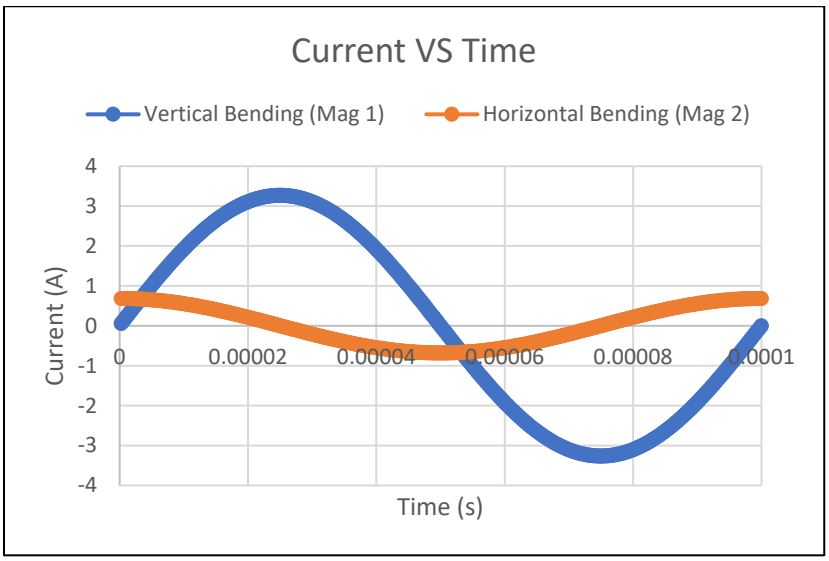

Figure 6 – Waveform to Produce the Ellipse in Figure 5

2.5.1.2 Square – Triangle Waveform

In Figure 7 a square raster pattern is shown with the corner points situated on the specified 100 mm maximum raster diameter. The corresponding waveforms associated with this pattern are seen in Figure 8. To create this pattern, each magnet must supply a steady triangle wave, 90 degrees out of phase from each other, at 10 kHz.

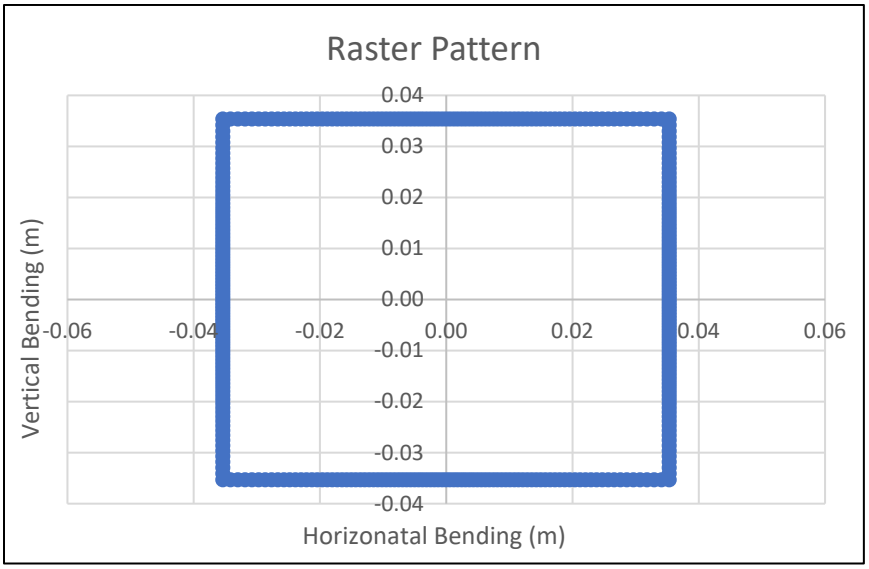

Figure 7 - Square Raster Pattern

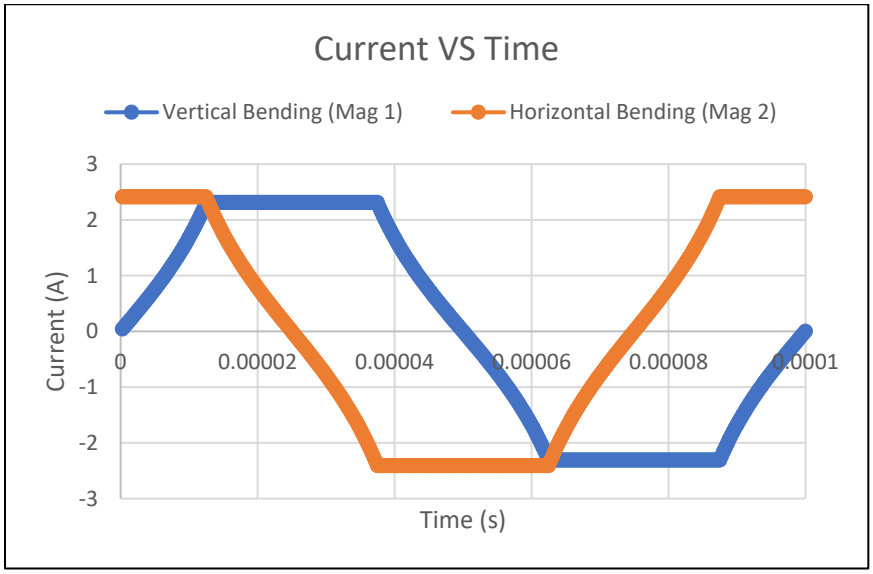

Figure 8 - Waveform to Produce the Square in Figure 7

To visually understand how the addition of harmonics affects the shape of this waveform, it is necessary to examine the Fourier series transform of a triangle wave. As stated above, it was determined to use a design frequency of 100 kHz, thus only the first ten harmonics were considered. Figures 9 to 12 show a triangle wave containing different harmonics with respect to the fundamental frequency. Through these graphical representations, it is possible to see how quickly the waveform converges on a triangle, and it is for this reason that rastering systems around the world typically choose this option.

$$Fourier\ Series\ Equation\colon\ -\frac{A}{2}\sum_{n=1}^{m}\frac{\cos\big((2n-1)2\pi Tx\big)}{(2n-1)^2} \qquad (1)^{9}$$

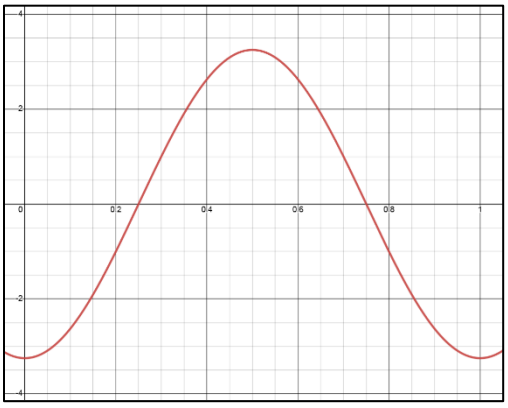

Figure 9 – Fundamental Frequency (m=1)

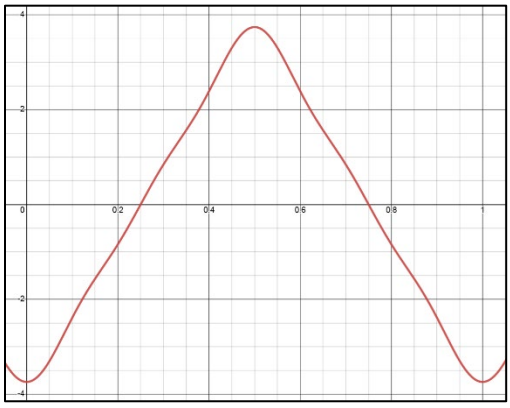

Figure 10 – 3rd Harmonic (m=3)

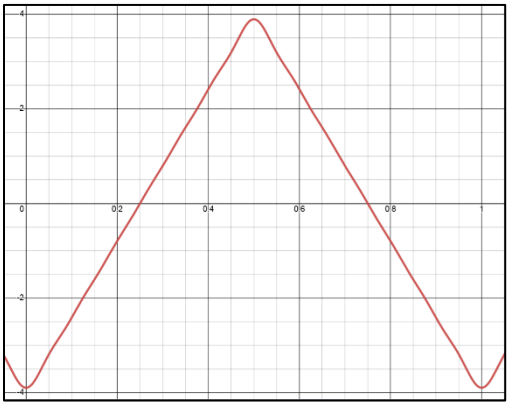

Figure 11 – 7th Harmonic (m=7)

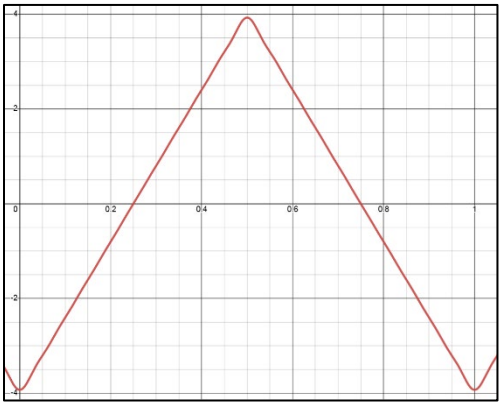

Figure 12 – 10th Harmonic (m=10)

[9] Fourier series equation for a triangle wave with amplitude (A) 6.5 and period (T) 1.

2.5.1.3 Strokes – Sawtooth Waveform

Figure 13 shows a proposed pattern that entails rastering strokes onto the target. This was an attractive option as the raster pattern could be synchronized with the pulse rate of the electron beam. Unfortunately, this is the most complicated pattern, in terms of harmonics, and requires a complex sawtooth wave. Figure 14 depicts the corresponding waveform to produce the stroked pattern in Figure 13. [10]

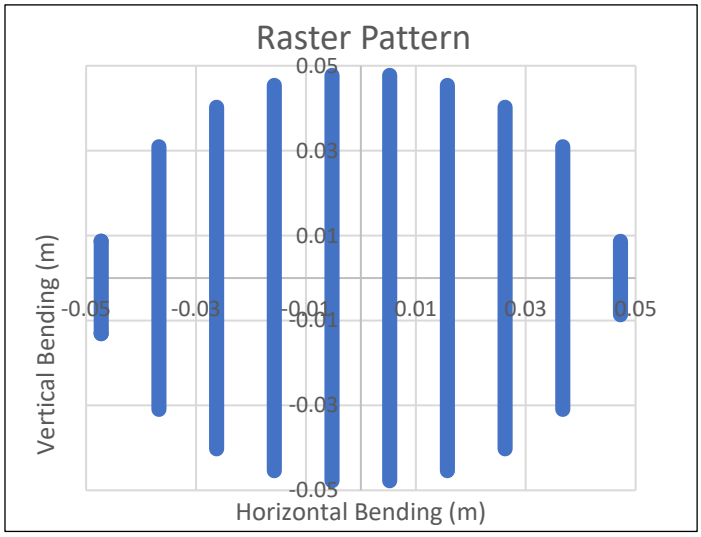

Figure 13 - Stroke Raster Pattern

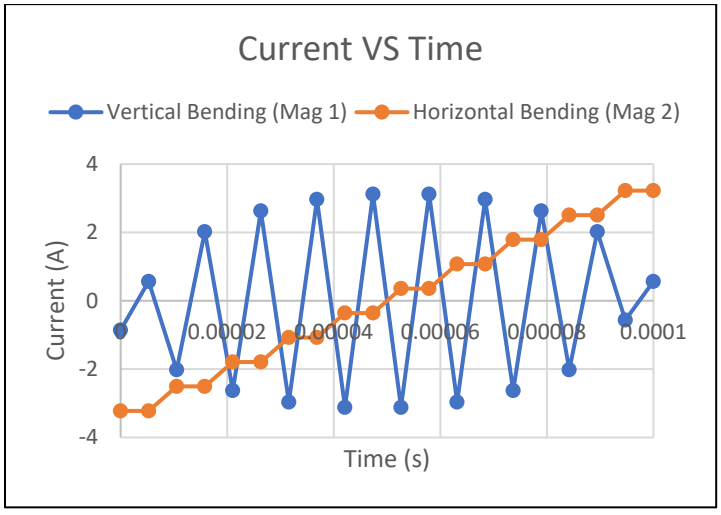

Figure 14 – Waveform to Produce Strokes in Figure 13

[10] Although the waveform for magnet 1 shows both a rise and fall, the pattern in Figure 13 shows only the rising portion. This is because the beam pulse has been synched with the waveform to only raster during the rise.

Figures 15 to 18 show a sawtooth wave containing different harmonics with respect to the fundamental frequency. Through the graphical representations, it is possible to see that even with the addition of 10 harmonics, there is still a relatively noisy waveform. It would require approximately 100 harmonics to approach a sawtooth wave that shows a sharp vertical drop-off.

Fourier Series Equation:

$$-\sum_{n=1}^{m}\frac{A}{\pi n}(-1)^n \sin\left(\frac{2}{T}\pi n x\right) \qquad (2)^{11}$$

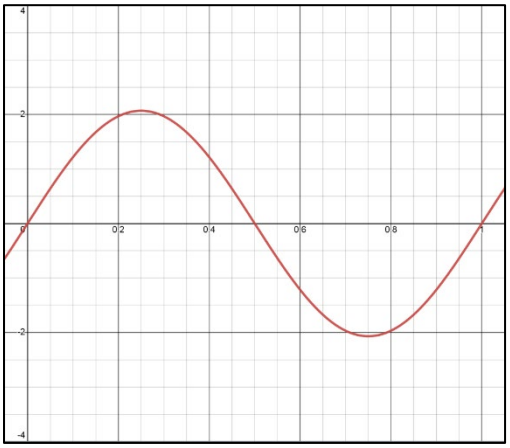

Figure 15 - Fundamental Frequency (m=1)

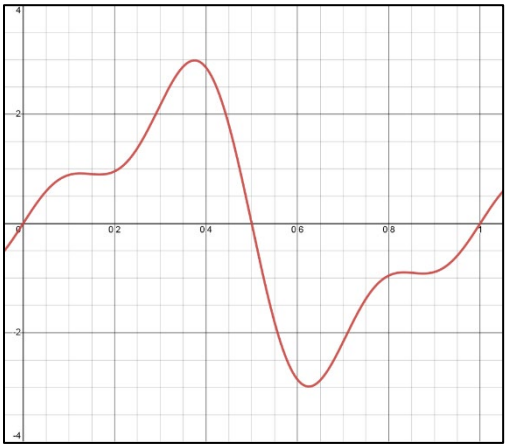

Figure 16 – 3rd Harmonic (m=3)

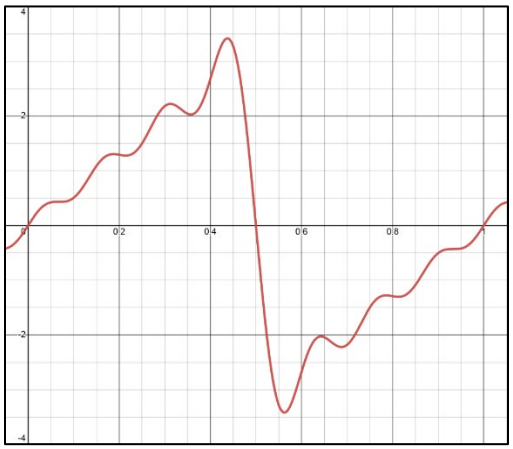

Figure 17 – 7th Harmonic (m=7)

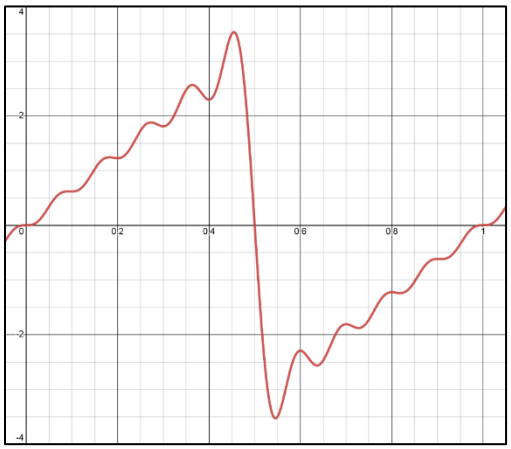

Figure 18 – 10th Harmonic (m=10)

[11] Fourier series equation for a sawtooth wave with amplitude (A) 6.5 and period (T) 1.

2.5.2 Discussion

Through the analysis of different raster patterns and waveforms, it seems the obvious choice would be a pattern that requires only pure sine or cosine waveforms. Unfortunately, due to the constraints with beam physics, including local heating, and uncertainty with target design and future requirements, it is likely that a more complex pattern will be required.

Triangle waves are what is typically seen in other raster systems around the world, such as the one at Berkley Laboratories discussed in Chapter 1. This is because with minimal harmonics, it is easier to create a triangle wave. In fact, most systems only consider the first 3 harmonics allowing for less stringent design criteria. In all likelihood, triangle waves will also be used for the raster system at TRIUMF.

Although the sawtooth wave does not seem like an attractive option with only ten harmonics, it is possible that this will be adequate for the purposes of target irradiation in ARIEL. Ultimately, 100 kHz was chosen as the design frequency to accommodate target uncertainty and the possibility of complex waveforms. The study and choice of raster patterns will be completed, in the future, as a separate physics project at TRIUMF.

Chapter 3 - Design

Divided into five sub-sections, this chapter details the design process for the two AC raster magnets. First, the magnetic field parameters are determined, followed by detailed design of the coils and core, a tabulation of the overall magnet parameters, and finally an overview of the vacuum tube.

3.1 Magnetic Field

As the goal of this project was to create electromagnets to raster an electron beam, it was first necessary to determine the required magnetic field for each magnet. The worst-case scenario of maximum beam deflection was used along with several assumptions. This section discusses the process to determine magnetic requirements.

Table 1 outlines three assumptions that were necessary in order to complete the subsequent calculations. First, an effective magnet length of 100 mm (0.1 m) was assumed and the corresponding distances from the target location were found based on an initial set-up and iterations following concept discussions at TRIUMF. Table 2 contains known values, and Figure 19 shows a screenshot from the SolidWorks model with relevant locational values.

Initial Assumptions	
Magnet Effective Length (L_{eff})	0.1 m
Distance from Target to First Magnet (L_1)	6.4099 m
Distance from Target to Second Magnet (L_2)	6.1372 m

Table 1 - Initial Assumptions

Known Values	
Maximum Electron Energy (E_b)	75 MeV
Electron Mass (m_0)	0.511 MeV/c^2
Maximum Raster Radius (r)	0.05 m
Speed of Light (c)	299,792,458 m/s

Table 2 - Given Values for Magnetic Calculations

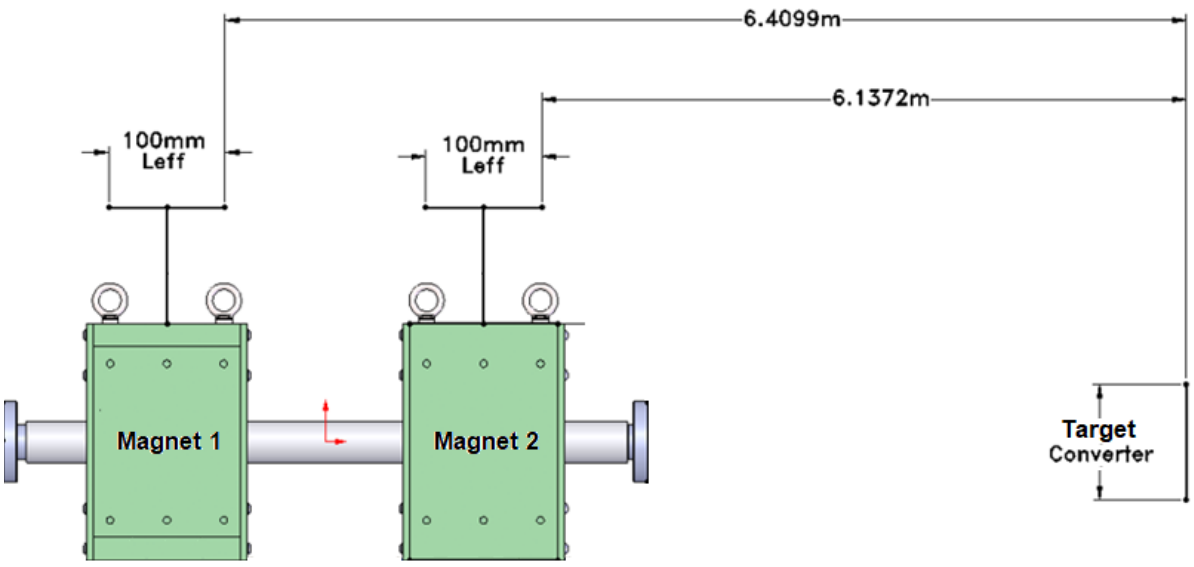

Figure 19 - Location of Magnets from Target & Effective Length

3.1.1 Magnetic Field Calculations

In order to determine the magnetic requirements, it was first necessary to calculate the magnetic rigidity. This is a measure of the bending radius of a particle (ρ) immersed in a magnetic field (B) and is defined as the ratio between the magnitude of particle momentum (p) to its charge (e) [12].

$$B\rho = \frac{p}{e} \tag{3}$$

Equation 3 can be rewritten, as seen in Equation 4, using the kinetic energy (E_k) [13] of the beam, and is a convenient way to determine the magnetic rigidity with the known variables.

$$B\rho = \frac{p}{e} = \frac{pc}{ec} = \frac{\sqrt{E_k^2 + (m_0c^2)^2}}{ec} \tag{4}$$

The kinetic energy of the beam was calculated using the following known formula [13].

$$E_K = E_b + m_oc^2 \tag{5}$$

$$E_k = 75\ MeV + \left(0.511\ {}^{MeV}/_{c^2}\right)c^2 = 75.511\ MeV$$

With the beam kinetic energy known, the magnetic rigidity was then calculated using Equation 4. The result is shown as

$$B\rho = \frac{\sqrt{{E_K}^2 + (m_o c^2)^2}}{ec} = \frac{\sqrt{(75.511x10^6 MeV)^2 + \left(\left(0.511x10^6\, {MeV}/{c^2}\right)c^2\right)^2}}{(1)(299{,}792{,}458\, {m}/{s})}$$

$$B\rho = 0.251883351\, Tm$$

From the magnetic rigidity value, using geometry, the bending radius could be determined. Figures 21 and 22 show these geometric sketches.

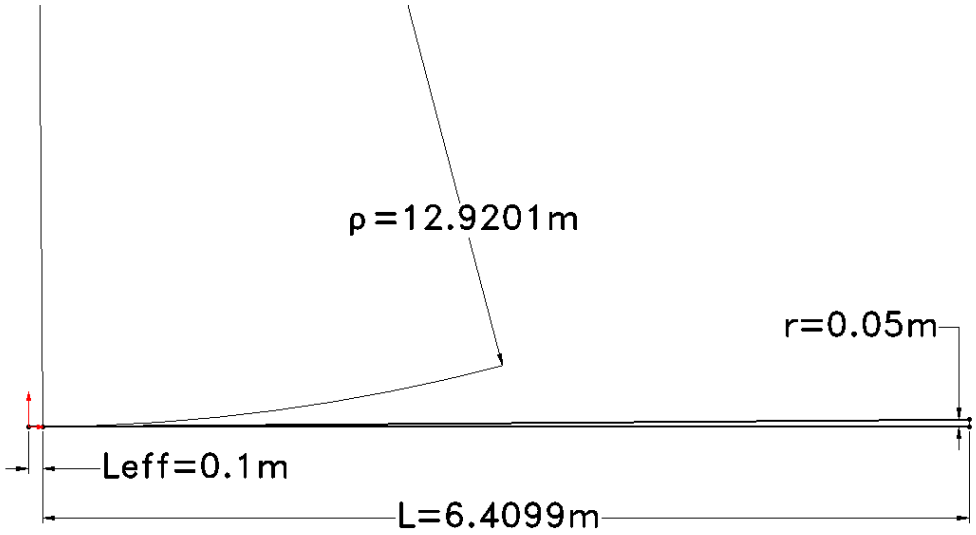

Figure 20 – Magnet 1 - Geometric Sketch to Determine Bending Radius

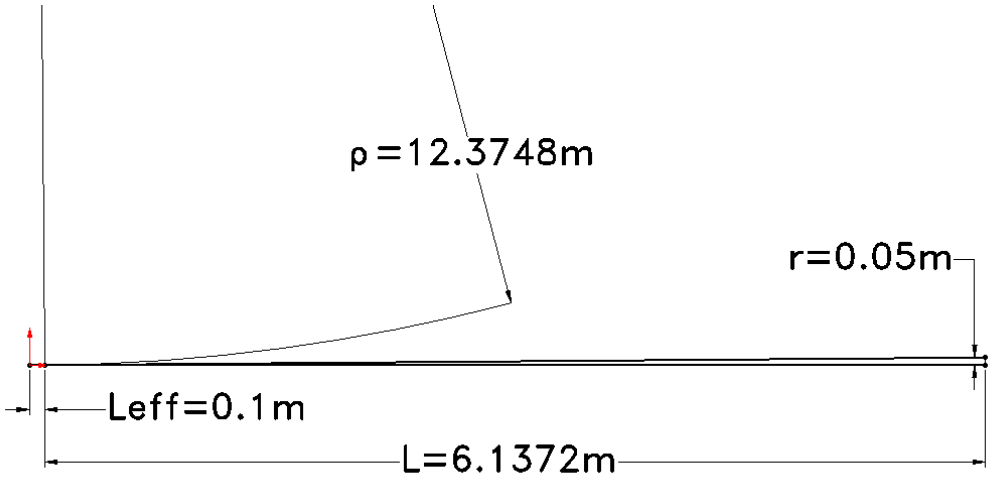

Figure 21 – Magnet 2 - Geometric Sketch to Determine Bending Radius

Finally, using the two known bending radii, the maximum magnetic fields, B_{Mag1} and B_{Mag2} were determined as follows.

$$B_{Mag1} = \frac{B\rho}{\rho_{Mag1}} = \frac{0.251883351\ Tm}{12.9201\ m} \tag{6}$$

$$B_{Mag1} = 0.0194955\ T = 194.955\ G$$

$$B_{Mag2} = \frac{B\rho}{\rho_{Mag2}} = \frac{0.251883351\ Tm}{12.3748\ m} \tag{7}$$

$$B_{Mag2} = 0.0203545\ T = 203.545\ G$$

3.2 Coils

With the magnetic field requirements known, design of the magnet coils could begin. As per requirement specification *RS 2.4.3*, the raster system will consist of two separate dipoles. This means that each magnet will have two coils connected in series. For this design, the worst-case magnetic field requirements, as calculated above, were considered. The following sections outline the design process for these coils.

3.2.1 Material

Standard materials used for conductors today are copper or aluminum due to their low resistivity, availability, and cost. In a conductor, the most important properties are the electrical resistivity and conductivity as they directly relate to size and performance. Some typical materials and their electrical properties are shown in Table 3.

Material	Resistivity (Ωm)	Conductivity (S/m)
Silver	1.59×10^{-8}	6.30×10^{7}
Copper	1.68×10^{-8}	5.96×10^{7}
Gold	2.44×10^{-8}	4.10×10^{7}
Aluminum	2.82×10^{-8}	3.5×10^{7}
Nickel	6.99×10^{-8}	1.43×10^{7}
Tin	1.09×10^{-7}	9.17×10^{6}
Stainless Steel	6.9×10^{-7}	1.45×10^{6}

Table 3 - Resistivity and Conductivity at 20°C for Common Materials [14]

Silver does show the highest conductivity with the lowest resistance, making it seem like an ideal choice but, aside from cost, silver tarnishes creating an oxide layer that is non-conductive [15]. This leads to copper with its high conductivity and low resistance. Copper can also be manufactured in varying grades, purities, and coatings. For these coils, 100% pure copper was chosen to allow for the highest current density with the smallest possible conductor cross-section.

3.2.2 Gap

In an electromagnet, the gap is the distance between the lower and upper poles and must be determined in order to continue with design. The required strength of the magnetic field is directly proportional to the gap size. As the gap increases, so do the field requirements and all associated components, thus it is preferable to have the smallest gap possible. For these magnets, the gap must clear the beam pipe, which consists of a 50.8 mm (2 in) outer diameter. To allow for clearance, manufacturing, ease of installation and alignment, a gap distance of 55 mm was determined.

3.2.3 Magnetomotive Force

Magnetomotive force (MMF) is analogous to electromotive force and is defined as the force that sets up the magnetic field within and around an object [16]. Measured in units of amp-turns, this can be thought of as the magnetic pressure that produces the magnetic field. If, for example, there was only one turn in the magnet coil, then the value of the MMF would be the amount of current that passes through the single turn to produce the corresponding magnetic field. The calculations for MMF of the two raster magnets are shown below, where *B* is the magnetic field, *g* the gap distance and μ_0 the permeability of free space [13].

$$MMF = \frac{Bg}{\mu_0} \tag{8}$$

$$MMF_{Mag1} = \frac{(0.0194955\ T)(0.055\ m)}{4\pi * 10^{-7}\ {}^{Tm}/_{A}} = \mathbf{853.2693\ A - Turns}$$

$$MMF_{Mag2} = \frac{(0.0203545\ T)(0.055\ m)}{4\pi * 10^{-7}\ {}^{Tm}/_{A}} = \mathbf{890.8697\ A - Turns}$$

3.2.4 Skin Depth

Alternating current has the tendency to flow along the outer surface of a conductor, known as the skin effect [19], and causes an increase in resistance. This distance, from the outer surface to where the current density falls to 1/e (approx. 37 %) of its surface value, is known as the skin depth [19], and this phenomenon is caused by eddy currents. Eddy currents, as defined by Lenz'z law [18], are closed loops of induced current flowing perpendicular to, and in opposition of, a changing magnetic field. The magnitude of the induced eddy currents is directly proportional to the area of the coil loop and frequency, and inversely proportional to the resistance [17]. Although concerning, the issues with respect to eddy currents and skin effect can be easily avoided by ensuring that current flows entirely though the cross-section of a conductor. To accomplish this, the diameter of the conductor selected must be smaller than the skin depth at the highest operating frequency.

The skin depth can be easily calculated, using Equation 9 [20], with the conductor material and frequency known. A calculation for the worst-case of 100 kHz is shown below with Table 4 containing values of skin depth at different frequencies from 1 kHz. For this application, the conductor must have a diameter smaller than 0.2063 mm.

$$\delta = \sqrt{\frac{2 * \rho_{cu}}{\omega * \mu_r * \mu_0}} = \sqrt{\frac{\rho_{cu}}{(\pi * f) * \mu_r * \mu_0}} \tag{9}$$

$$\delta_{100000} = \sqrt{\frac{0.0000000168}{(\pi * 100000) * 0.999994 * (4\pi * 10^{-7})}}$$

$$\delta_{100000} = 0.000206289\, m = 0.206289\, mm$$

Skin Depth for 100 % Copper	
Frequency (Hz)	Skin Depth (mm)
1000	2.062890023
2000	1.458683524
3000	1.191010110
4000	1.031445011
5000	0.922552464
6000	0.842171325
7000	0.779699140
8000	0.729341762
9000	0.687630008
10000	0.652343103
100000	0.206289002

Table 4 - Skin Depth of Copper w.r.t Frequency

3.2.5 Conductor

Magnets that operate at room temperature and do not use active cooling, such as a water channel through the middle of the conductor, must limit the current density to a maximum of 2 A/mm^2 [21]. This prevents overheating of the conductor which can lead to a change in the material properties and a breakdown of any insulation. According to the skin depth calculations in the previous section, the conductor must be smaller than 0.206 mm which corresponds to a standard wire size of 33AWG (0.1798 mm). To determine if this is a suitable solution, the number of turns required based on maximum current density was calculated using Equations 10 and 11.

The current associated with a maximum of 2 A/mm^2 was calculated using the following formula, where I is the current, J the current density and A the cross-section of the conductor [21].

$$I = J * A \tag{10}$$

$$I = \left(2\,{}^{A}/_{mm^2}\right) * \left(\frac{\pi}{4}0.1798^2\right) = 0.0508\ A$$

The number of turns associated with the above maximum current value and magnetomotive force was calculated as follows.

$$\#\ of\ turns\ (N) = \frac{MMF}{I} \tag{11}$$

$$N = \frac{890.8692\ A - turns}{0.0508\ A} = 17{,}536\ turns$$

It is quickly apparent that this is not a suitable solution. With over 17,000 turns, the total length of copper, and size of the coil, would be unreasonable. One option would be to add a cooling channel to increase the conductor cross-section or turn to super-conducting magnets. Fortunately, there is an alternative choice for the conductor specifically designed for high frequency applications called litz wire and it is discussed in the following section.

3.2.5.1 Litz Wire

Litz wire, derived from the German word “litzendraht”, meaning woven strands, was developed in the late 1800’s for high frequency applications. litz wire is manufactured by twisting many thin insulated wires together in a specific pattern. The diameter of these wires being smaller than the skin depth eliminates any skin effects issues [23]. Another issue caused by AC current in a coil is the proximity effect. Similar to the skin effect, discussed in the previous section, the proximity effect refers to the magnetic field generated in each separate conductor in a coil. The alternating magnetic field creates eddy currents in the adjacent winding causing the overall current distribution to concentrate as far away as possible from the nearby conductor. This creates unwanted heat and can increase the resistance of the coil by a factor of ten. Litz wire mitigates this by twisting each conductor to ensure they are equally along the outside and inside of the cable causing the current to spread uniformly [26]. Figure 22 shows a sample of a twisted litz wire bundle. It is for these reasons that litz wire is the ideal choice of conductor for these coils. The following sections outline the process of litz wire selection.

Figure 22 - Litz Wire Sample

1. *Diameter of single wire (d_w)*

   As discussed in Section 3.2.4, the conductor diameter must be less than the worst-case skin depth of, in this case, 0.206 mm at 100 kHz. For litz wire, it is recommended to choose a wire diameter of approximately one third the skin depth [22].

$$d_w = \frac{\delta}{3} = \frac{0.206\ mm}{3} = 0.068\ mm \tag{12}$$

   Since 0.068 mm is a non-standard size, the closest standard wire diameter of 0.08 mm was selected.

2. *Number or single wire strands (n_s)*

   With the single wire diameter selected, the total number of strands can be calculated by considering the cross-sectional area of a single strand and the maximum current density of 2 A/mm^2.

$$A_{sc} = \left(\frac{\pi}{4}\right) 0.08\ mm = 0.005027\ mm^2$$

$$n_s = \frac{J}{A_{sc}} = \frac{2\ {}^{A}/_{mm^2}}{0.005027\ mm^2} = 398\ strands \tag{13}$$

   For convenience of litz wire construction, a total of 400 strands was selected.

3. *Insulation & Serving*

   In standard litz wire applications, each individual wire is insulated with a coating and once wound, the entire bundle is wrapped, or served, with an external insulator. These can be a variety of materials, such as nylon, polyester, and polyamides [22]. Unfortunately, due to the radiation requirement of 2.6 x 10^5 Gy, standard insulators are insufficient for the lifetime of the coil. To mitigate this issue, a new form of litz wire using ethylene tetrafluoroethylene (ETFE) will be used. ETFE has a radiation resistance up to 5 x 10^5 Gy [25], almost double the requirement. Developed by

Dupont®, ETFE is a fluoropolymer in the same family as Teflon and has excellent mechanical, electrical, and chemical properties. See *Appendix A* for a full table of ETFE properties.

New England Wire Technologies has created an insulated litz wire using ETFE specifically for conductor applications known as NEWind® [25]. NEWind® uses thin layers of extruded ETFE insulation to ensure good electrical insulation between each wire, bundle and ultimately each turn in the final coil.

4. *Construction*

Litz wire construction is classified into eight basic types, each type incorporating the previous type. For example, Type 1 litz wire is simply any number of single conductors twisted together. Type 2 would then take several of the twisted Type 1 strands and twist them together. Type 3 again twists the resulting Type 2 wires together. Types 4, 5, and 6 follow this same approach but with the addition of a central fibre core and Types 7 and 8 are rectangularly compressed versions [25].

It has been shown that the optimal number of final twisting operations must be an integer of the total number of strands and is typically 5 or 7 [28]. Figure 23 shows a 5 bunched, Type 1, litz wire bundle. For the final bunching operation of the 400-strand litz wire specified, 5 bundles of 80 strands are ideal.

Figure 23 - 5 Bunched, Type 1, litz Wire Bundle

To determine the number of preceding bunching operations, the maximum number of strands in the first bunch was first calculated using Equation 14 [28], with $n_{1,max}$ the maximum permissible strands, δ the skin depth and d_w the diameter of a single wire.

$$n_{1,max} = 4 * \frac{\delta^2}{d_w^2} = 4 * \frac{(0.206\ mm)^2}{(0.08\ mm)^2} = 26.52\ \approx 27 \tag{14}$$

Since, 27 is not an integer multiple of 80, and it has been shown that bunching in groups of 5 is an optimal solution, 16 strands were chosen for the first bunching step. This leads to a Type 2 construction consisting of 5 twisted bunches of 16 wires, creating 5 bunches of 80, that are then twisted together again for a total of 400 twisted strands. Figure 24 shows examples of this construction.

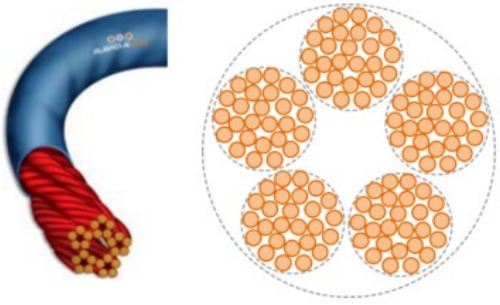

Figure 24 - Type 2, 5 Bunched litz Wire Bundle

For an optimal current distribution, the length of lay, measured in twists per meter, should be approximately 25 times the outer diameter of the bundle. This equates to 100 mm (25 x 4 mm), or 10 twists per meter [11]. This may be further optimized with the wire manufacturer and their parameters.

5. *Overall diameter*

Although the actual outer diameter may vary slightly due to the manufacturing process and the inherent flexibility of litz wire, an estimation of the total overall diameter can be done using Equation 15, where n_{sw} is the number of single wires, d_{sw} the diameter of

a single wire, t_i the thickness of insulation, and k_{pf} the packing factor which equals 1.28 for any number of wires between 20 through 400 [25].

$$OD_{LW} = k_{pf} * \sqrt{n_{sw}} * (d_{sw} + 2t_{0c}) \quad (15)$$

$$OD = 1.28 * \sqrt{400} * \left(0.08\,mm + 2(0.0381\,mm)\right) = 3.9987\,mm$$

$$OD \approx 4 \text{ mm}$$

3.2.5.2 Conductivity Comparison

Litz wire is not ideal for DC applications as there are no issues with eddy current formation due to the skin effect. This means that the current will occupy the entire cross-section of the conductor. For example, a copper wire with a diameter of 4 mm would have a total conductivity of approximately 747 S/m, whereas a litz wire bundle with the same overall diameter would only contain a copper cross-section of approximately 2.02 mm^2, and thus a conductivity of 120 S/m.

This same comparison considering AC at 100 kHz changes the cross-sectional area of the copper wire to only the area contained within the skin depth of 0.20629 mm. The conductivity would then only be approximately 145 S/m, a drastic reduction due to the skin effect.

Although it seems a solid copper wire still allows for the greatest conductivity, as discussed in Section 3.2.4, the conductor diameter must be smaller than the skin depth.

3.2.6 Winding Parameters

The next sections outline the winding parameters of the coils with the overall length and width determined by the core dimensions discussed in Section 3.3.

3.2.6.1 Number of turns

The number of turns per coil was determined by using Equations 10 and 11 with the maximum current and MMF values.

$$I = \left(2\,{}^{A}/_{mm^2}\right) * (0.005027\ mm^2 * 400\ strands) = 4.0216\ A$$

$$N = \frac{890.8692\ A - turns}{4.0216\ A} = 221\ turns$$

With a maximum current of 4.0216 A, the required number of turns is 221, but, since there are two coils, an even number of turns should be selected. In this case 228 turns were selected for 2 coils consisting of 114 turns each. The next section shows that 228 is an optimal choice for the winding window.

3.2.6.2 Winding Window & Pattern

For an optimized coil, using a round conductor, an orthocyclic winding pattern gives the highest fill factor at 90.7% [29]. This pattern has the windings of each subsequent layer placed into the grooves of the previous layer. Figure 25 shows an example of an orthocyclic winding pattern.

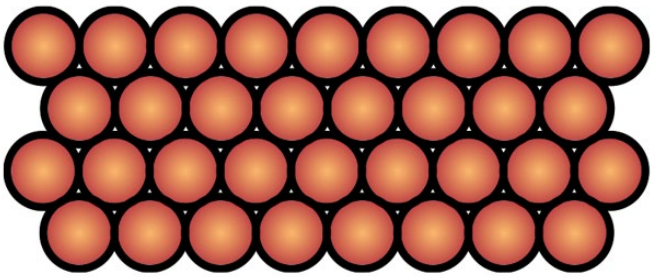

Figure 25 - Orthocyclic Winding Pattern

With the winding pattern selected, the winding window could be determined by looking at different combinations of numbers adding to 114. It was found that a winding pattern consisting of 6 layers of 10 and 6 layers of 9, gives a relatively square window and, through simulations[12], an optimal magnetic field. Figure 26 shows a sketch of the winding pattern within the winding window.

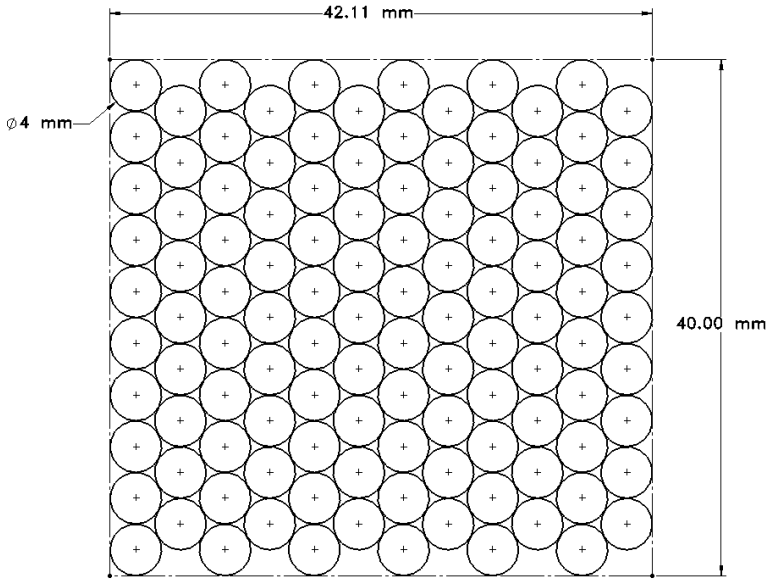

Figure 26 - Winding Window with Pattern

3.2.6.3 Bobbin

The conductor is wound around a bobbin to ensure the tight packing and winding profile does not change during the operational lifetime of the magnet. It is also convenient for maintenance

[12] Simulations are discussed in Chapter 4

should there be any issues with the coil and a need for replacement. Typically, conductors are wound around a temporary bobbin while being wrapped with insulation and then impregnated into a resin mold. Since the selected litz wire is already insulated with a radiation resistant material, there is no need for resin impregnation or any other insulation. This leads to an open-air, 3D printed, bobbin. The most challenging requirement is the material selection as the radiation is quite high. Fortunately, with constant improvements in 3D print technology, polyphenylene sulphide (PPS) can now be printed. PPS, as seen in Figure 27, has a very high resistance to radiation with 10^7 Gy, two orders of magnitude higher than *RS 2.1.1.*

Organic Materials	Radiation Dose Limits
Polyether-ether-ketone (PEEK) Polyetherimide (PEI) Glass or carbon fibre filled resins: - Epoxy, aromatic hardener - Phenolic - Polyester - Polyimide (PI) - Polyurethane (PUR) - Polyphenylene sulfide (Ryton®, PPS) - Polyphenylene oxide (PPO) - Silicone	10^7 - 10^8 Gy

Figure 27 - Radiation Dose Limits in Air for Common Polymers [30]

A screenshot of the conductor wound around a 3D printed bobbin is shown in Figure 28. As mentioned above, the overall dimensions are discussed in the following section on core design.

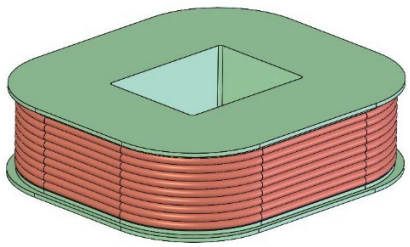

Figure 28 - SolidWorks Screenshot of Conductor on 3D Printed Bobbin

3.3 Core

The main purpose of a core in an electromagnet is to link the two magnet coils together through the non-magnetic gap by providing an easy path for the magnetic flux. With this concentration of magnetic field lines, it also facilitates the production of a higher magnetic field than that of a coil in air [33]. This section outlines the material selection and design of the magnet core with further explanation on the pole profile provided in the subsequent chapter on simulations.

3.3.1 Material

When considering materials for magnets, the property of interest is the permeability. This is a measure of the material's ability to become magnetized and is separated into three distinct categories: diamagnetic, paramagnetic, and ferromagnetic. Diamagnetic materials exhibit a negative susceptibility to magnetic fields, such as copper, silver, or gold whereas paramagnetic materials have a slightly positive susceptibility. Although slightly magnetic, paramagnetic materials do not retain any magnetic properties when removed from the source, such as magnesium or tantalum. The third category, ferromagnetic, contains materials that have a large susceptibility and typically retain their magnetic properties even after being removed from the source, such as iron, nickel, and cobalt [34]. Ferromagnetic materials are the optimum choice for any inductor and can have a permeability anywhere from 20 to 20,000 [34]. To quantify this value, the permeability of a material is considered relative to the permeability of free space and can be calculated using Equation 16 [33], where μ is the permeability of the material and μ_0 the permeability of free space. A material with a relative permeability of less than 1 is considered diamagnetic, paramagnetic materials are very slightly higher than 1 and anything much greater than 1 is considered ferromagnetic. Typical electromagnet cores are manufactured from AISI C1006 or C1010 Steel [33].

$$\mu_r = \frac{\mu}{\mu_0} \tag{16}$$

A material's permeability is not constant and changes with the magnitude of the magnetic field, thus it is necessary to look at B-H curves[13]. Figure 29 shows the B-H curve for C1006 and the magnified area of interest for this design.

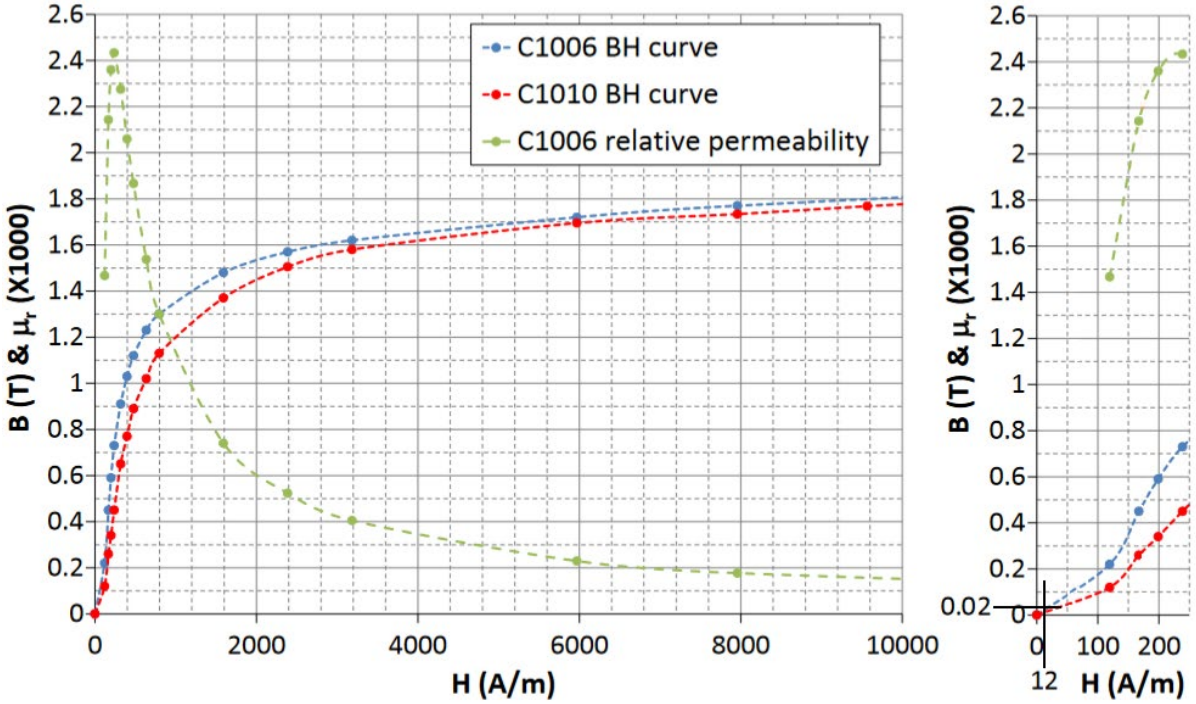

Figure 29 – B-H Curves for AISI C1006 and C1010 Steel (Left) & Magnified Area of Interest (Right) [32]

The relative permeability for C1006 steel can be calculated with Equation 17 [35], using the values extracted from the B-H curve above.

$$B = \mu_r \mu_0 H \tag{17}$$

$$\mu_r = \frac{B}{H * \mu_0} = \frac{0.02\ T}{\left(12\ {}^{A}/_{m}\right) * \left(4\pi * 10^{-7}\ {}^{H}/_{m}\right)} = 1326.29$$

[13] B-H curves show the magnetic flux, *B*, vs the magnitude of the magnetizing force *H*.

As with the copper conductor in the coil, AC current also causes eddy currents to form in the magnet core, creating similar skin effect issues. To avoid this, the skin depth of the core material must also be considered. With the relative permeability known, the skin depth can be calculated using Equation 9. The calculation for worst-case skin depth at 100 kHz is shown below with results from 1 to 100 kHz tabulated in Table 5.

$$\delta_{100000} = \sqrt{\frac{0.000000174}{(\pi * 100000) * 1326.29 * (4\pi * 10^{-7})}}$$

$$\delta_{100000} = 0.00001822953\ m = 0.01822953\ mm$$

Skin Depth for AISI C1006 Steel	
Frequency (Hz)	Skin Depth (mm)
1000	0.182295315
2000	0.128902254
3000	0.105248249
4000	0.091147658
5000	0.081524943
6000	0.074421751
7000	0.068901153
8000	0.064451127
9000	0.060765105
10000	0.057646840
100000	0.018229532

Table 5 - Skin Depth of AISI C1006 Steel w.r.t Frequency

In applications with a lower frequency such as transformers or CRT televisions, the core can be manufactured from a series of laminated thin sheets that are smaller than the skin depth. For example, a 60 Hz transformer would only require laminations thinner than 0.75 mm. Unfortunately, at the higher frequencies, this is not a viable option as it is not possible to manufacture laminated sheets smaller than the 0.018 mm skin depth.

This leads to the selection of ferrite for the core material. Ferrite is a polycrystalline ceramic-like material composed of iron oxide and other metals, typically nickel-zinc or manganese-zinc [36]. Formed by reacting iron oxide with other metals, ferrites provide a high permeability material consisting of crystals that are much smaller than the skin depth [36], effectively eliminating the formation of eddy currents. This makes ferrite ideal for any high-frequency inductor.

A medium permeable ferrite from Magnetics [37] was selected for these magnet cores. Their J-Material provides a constant permeability of 5000 through the design frequency, as seen in Figure 30, and a saturation flux density[14] of more than double the required field. The properties of J-Material are shown in Table 6, with B-H loops in Figure 30. It is important to note the curie temperature of 145 ºC, as the magnetic properties are removed beyond this value. See Figure 31 for further details. The remanence of 100 mT is not concerning as the required magnetic field for this application is approximately 20 mT. These ferrite blocks are manufactured with maximum dimensions of 104 x 66 x 18 mm^3; thus, a set of blocks will be bonded together using an epoxy and then machined to the final profile.

[14] Saturation flux density is the maximum amount of magnetic field that can be applied to a material.

Initial Perm (10 kHz)	5,000 ± 20%
Saturation Flux Density (4,300 G at 15 Oe, 25°C)	430 mT, 11.9 A•T/cm
Curie Temperature	145°C
Maximum Usable Frequency (50% roll-off)	≤0.7 MHz
Relative Loss Factor (tan δ/μ_{iac}) $X10^{-6}$, 25°C	≤15 (100 KHz)
Remanence (1,000 G, 25°C)	100 mT
Resistivity	0.5 Ω-m
Density	4.8 g/cm^3

Table 6 - Properties of J-Material Ferrite from Magnetics

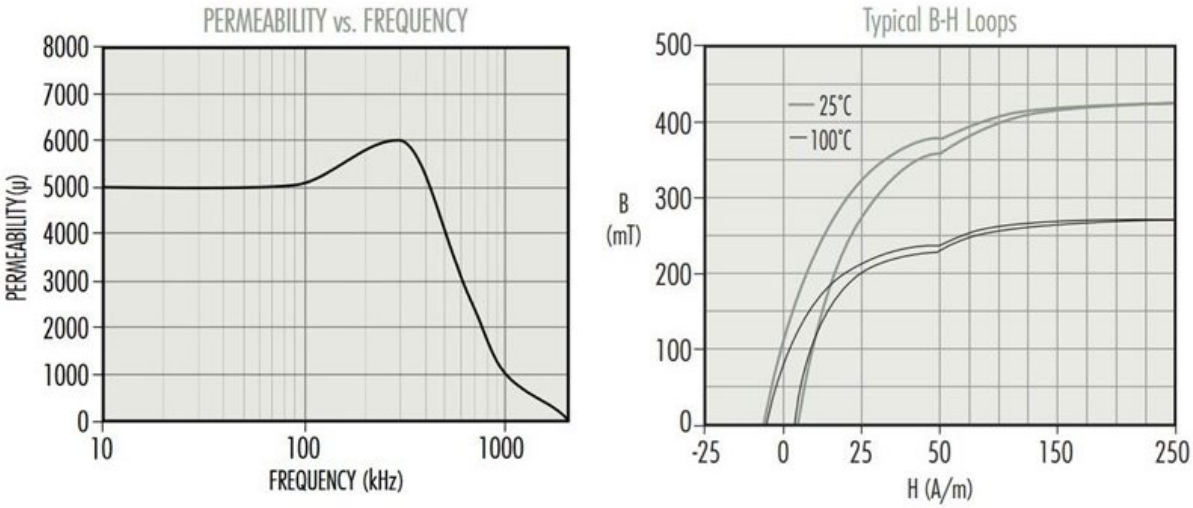

Figure 30 - Permeability w.r.t. Frequency, and B-H Loops for J-Material Ferrite

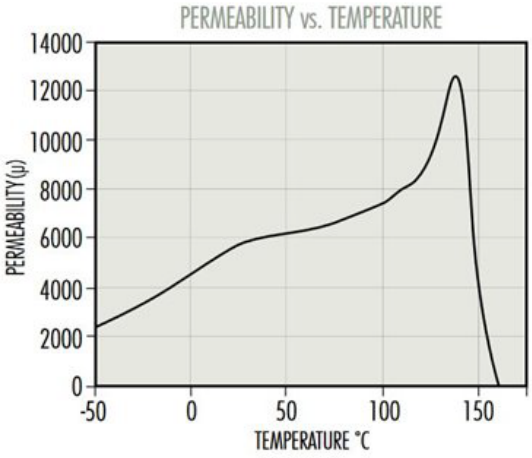

0

Figure 31 - Permeability w.r.t. Temperature for J-Material Ferrite

3.3.2 Shape & Dimensions

An H-frame profile will be used for the magnet core as it provides a uniform, symmetrical magnetic field [38]. Figure 1, in the Introduction, shows an example of an H-frame dipole magnet.

Initial dimensioning of the magnet core was determined by considering the winding window from Section 3.2.6.2 and the pole gap of 55 mm. Figure 32 shows initial dimensioning of the core with a pole height equal to the winding window plus additional clearance for the 3D printed bobbin. It has been shown that a core thickness equal to the pole height provides a good starting point which can be further optimized through simulations [38]. The pole profile was considered as a flat square and iterated during simulations to provide the required field, see Section 4.3.

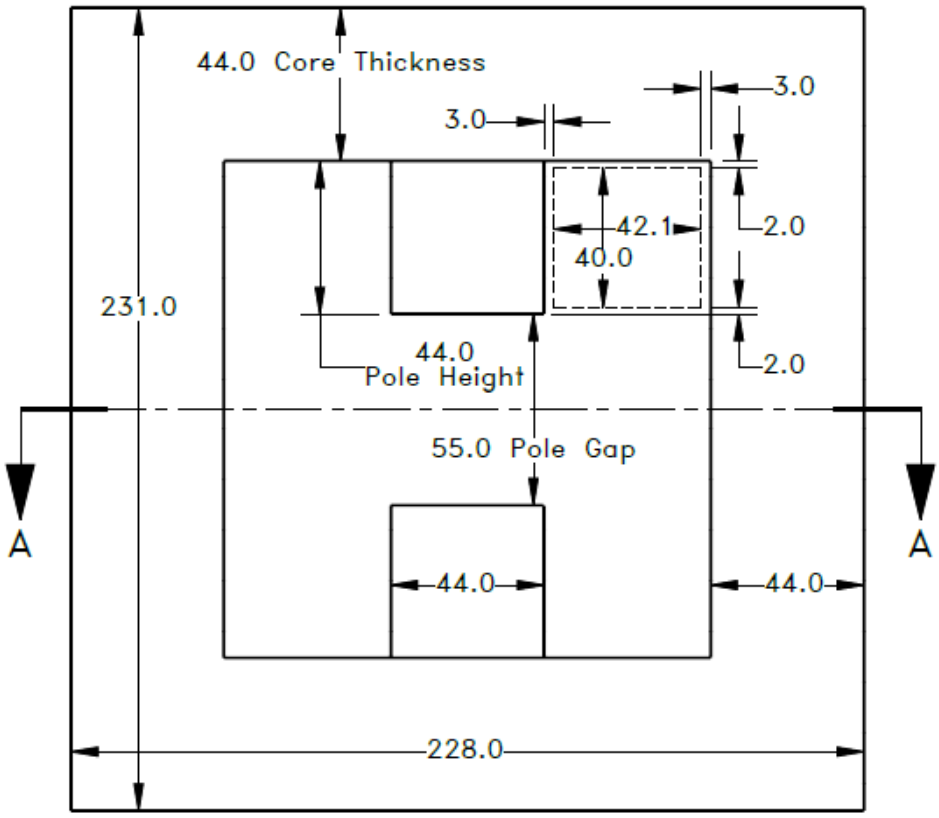

Figure 32 - Initial Core Dimensioning - Front View
(Dimensions are in mm; Scale 1:2.5)

The same procedure was used to determine the initial overall length. Figure 33 shows a sectioned top-view of the magnet core. The initial pole length was arbitrarily chosen as 75 mm and iterated during simulations, see Section 4.3.

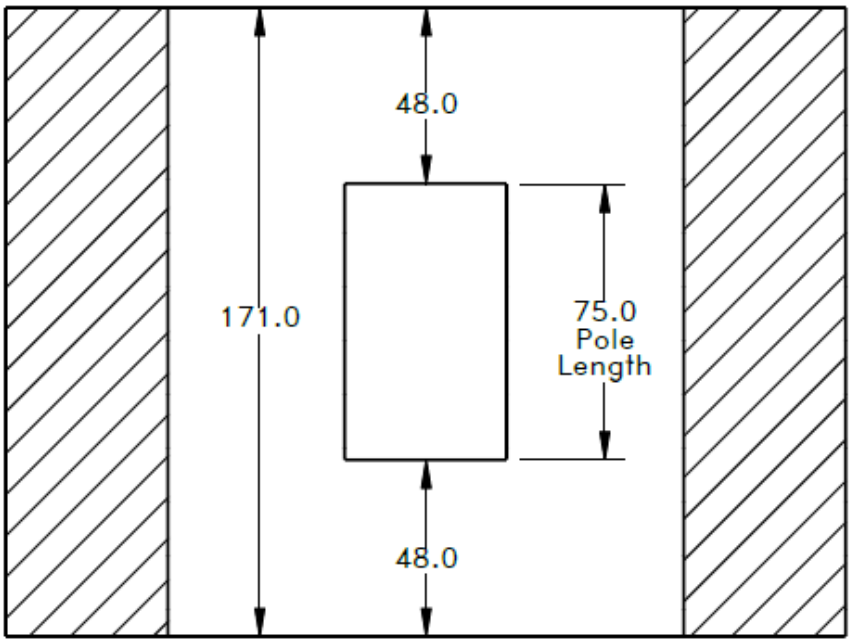

Figure 33 - Initial Core Dimensioning - Section A-A
(Dimensions are in mm; Scale 1:2.5)

Electromagnet design is an iterative process that requires complex computer simulations to fully determine the shape and profile of the core. With a baseline set of dimensions, as outlined above, it was then possible to optimize through simulations. This process is discussed in Chapter 4 – Simulations.

3.4 Outer Casing

The entire magnet will be held together with an outer casing to prevent the need for any fastening through the ferrite material, and to allow for assembly into the existing beamline. Unfortunately, the outer casing is susceptible to the same eddy current issues seen in the coil and core, and can adversely affect the functionality of the magnet, thus it is ideal to choose a material that is non-magnetic, such as a thermoplastic or thermoset. Again, the radiation resistance must be considered, and extensive testing has been completed by CERN in this regard [30]. Figure 34 shows the radiation resistance of common thermosets with the addition of PEEK. Polyetheretherketone is a common material used for high radiation applications due to its mechanical properties and ease of machining; unfortunately, PEEK is very expensive. For a more cost-effective solution, approximately six times cheaper, a phenolic[15] glass laminate thermoset was selected. G11 exhibits excellent electrical and mechanical properties, machinability, radiation resistance and cost. See Appendix A for a specification sheet.

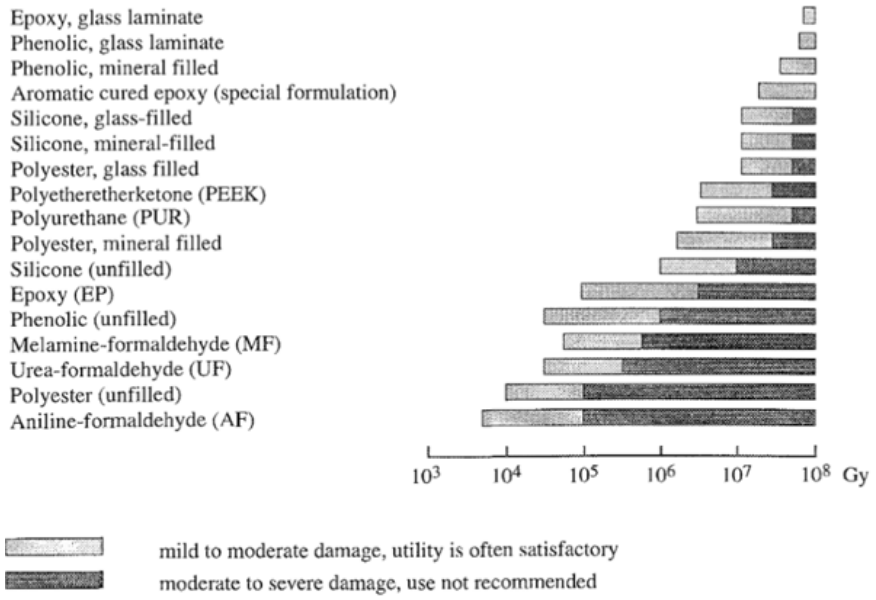

Figure 34 – Radiation Resistance of Thermoset Resins with the Addition of PEEK

[15] A phenolic material is created by using layers of cotton, paper, or a mix of glass fabric, placing them under heat and pressure and filling with synthetic resin [31].

3.5 Vacuum Tube

The final component to be considered in this raster system is the vacuum tube. This must seamlessly integrate into the existing beamline which consists of standard 2" OD tubing, a DN 50 CF flange at either end, and a nominal gap of 592 mm. Figure 35 shows a model of the beampipe location in the existing beamline.

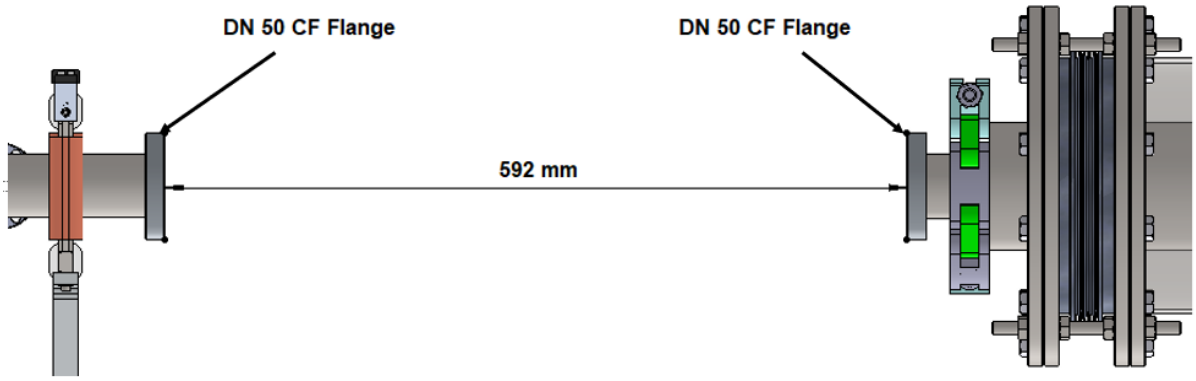

Figure 35 - Raster System Beampipe Location

Since the beampipe cannot be magnetic, there are a limited number of material choices as again, the radiation resistance is an issue. In typical accelerator applications, insulating beampipes are manufactured from ceramic materials. As such, an aluminum oxide ceramic material will be used for this beampipe. FRIALIT F99.7 from Kyocera has been used for beampipes at accelerator facilities all over the world [41]. A specification sheet for FRIALIT F99.7 can be found in Appendix A. A DN 50 CF flange shall be brazed to either end via a Kovar sleeve.

Due to the insulating properties of the ceramic material, beam induced charges will build-up along the inner wall of the ceramic. This can lead to mis-steering of the electron beam and strong discharges [6]. To prevent this, the inner surface of the beampipe shall be metalized

with a layer of either nickel or titanium, smaller than the skin depth; 0.001 mm for Ti and 0.01 for Ni. Figure 36 shows a model of the beampipe.

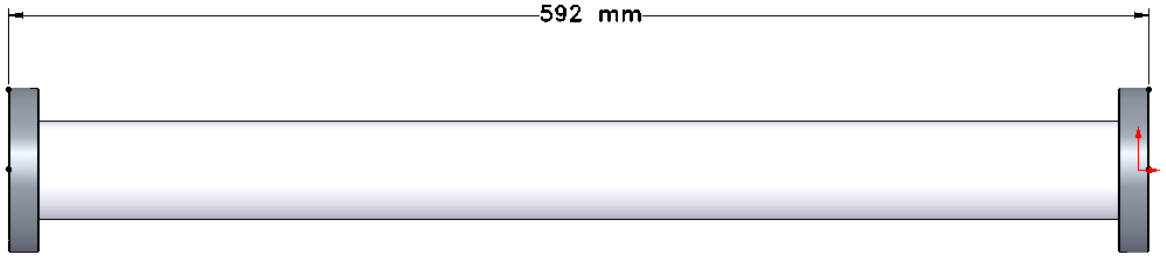

Figure 36 - Beampipe Assembly

Chapter 4 – Simulations

With the advent of technology, computer simulation software has become a standard tool in engineering design, and there are several electromagnetic simulation programs on the market today. For this project *Dassault Systèmes OPERA 3D* was used as it is the standard software for magnet design at TRIUMF. Section 4.1.1 shows an example. This chapter outlines the approach and subsequent simulations completed to optimize the magnet design.

4.1 Approach

When simulating an electromagnet, there are two main variables to be considered, the first is the magnetic field produced and the second is the field integral. To understand the field integral, consider a probe approaching the magnet along its centre axis from negative infinity. The magnetic field will slowly rise as the probe approaches the centre point, where it will reach its maximum, and then fall as the probe continues away towards positive infinity [21]. The effective length (l_{eff}) is defined as the integrated magnetic field, from negative to positive infinity, over the central magnetic field; see Equation 18. The actual steel length will always be smaller than the effective length [21].

$$l_{eff} = \frac{\int_{-\infty}^{\infty} B(z)dz}{B_o} \tag{18}$$

The integrated field is very difficult to calculate analytically and is determined using numerical computation. Since the maximum magnetic field, calculated in Section 3.1.1, is known and the effective length has already been chosen as 0.1 m, Equation 18 can be rearranged to give the required field integral as shown in Equation 19.

$$\int_{-\infty}^{\infty} B(z)dz = l_{eff} * B_0 \tag{19}$$

$$\int_{-\infty}^{\infty} B(z)dz = 0.1\ m * 0.02047176\ T = 0.002047176\ Tm$$

With the value of this field integral known, the magnet can be simulated in OPERA to determine the optimal dimensions that yield the required integral and magnetic field.

As per *RS 2.3.2*, the magnets must be compatible with a beam diameter of 25 mm, this means the magnetic field, and field integral must be homogeneous within this area. As such, three field lines along the *z*-axis from -500 mm to +500 mm, were considered; centre and +/-12.5 mm off axis. The +/- 500 mm field line distance corresponds to the 500 mm^3 boundary box discussed in Section 4.2. Figures 37 and 38 show SolidWorks models of this area of interest.

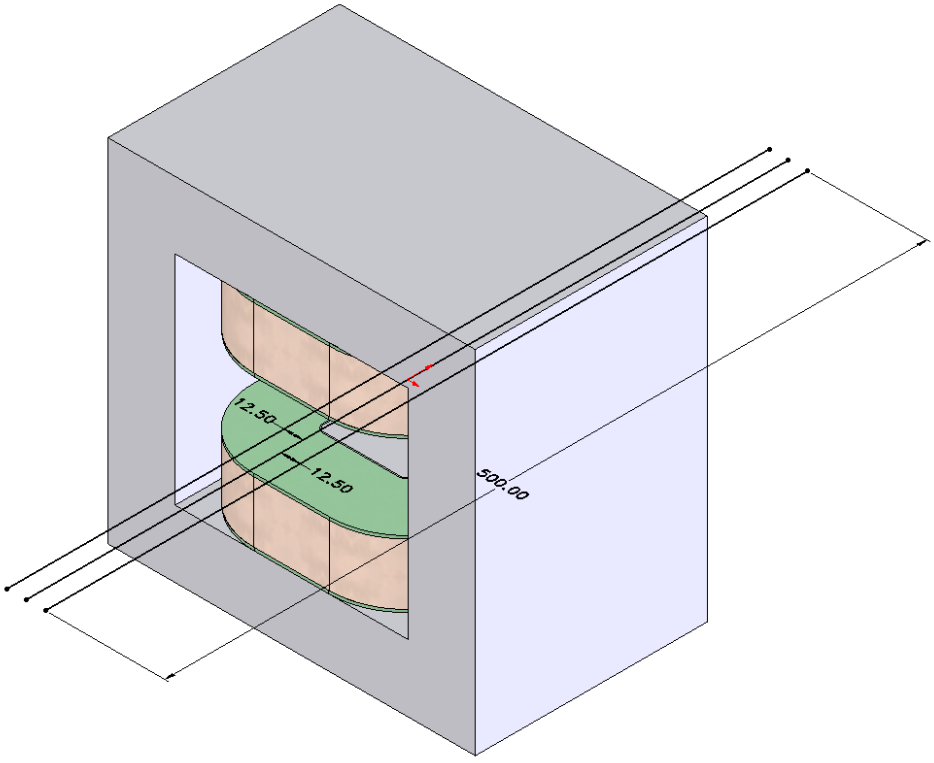

Figure 37 - Area of Interest for Simulation - Field Lines

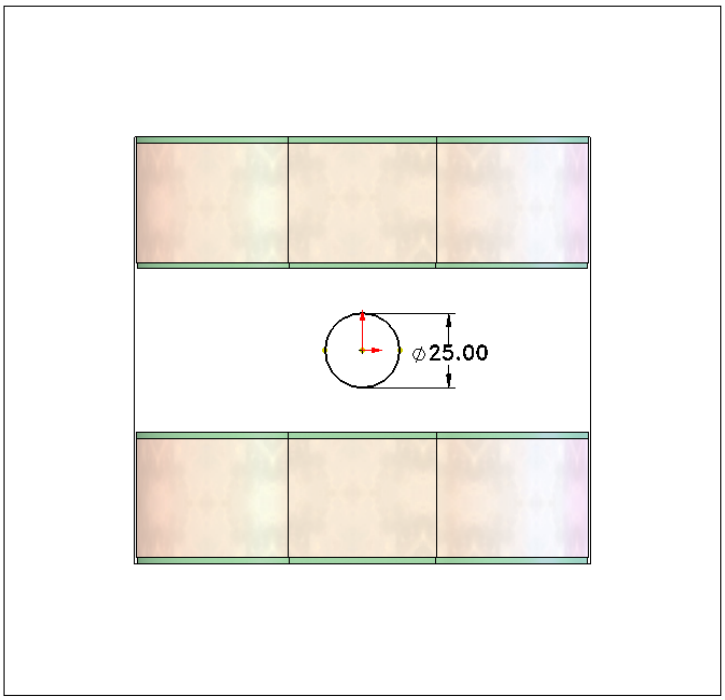

Figure 38 - Area of Interest for Simulation - Beam Window

4.1.1 OPERA example

OPERA Electromagnet and Electromechanical Simulation software is widely used for electromagnet simulations and is the standard software at TRIUMF. Magnets at TRIUMF are also mapped to verify that they match the simulated data. Figure 39 shows a simulated vs mapped field integral for a steering magnet with a maximum error of approximately 0.6%. A small error is expected due to the inherent nature of simulations vs realistic conditions and is accounted for by adjusting the input current to meet the required magnetic field.

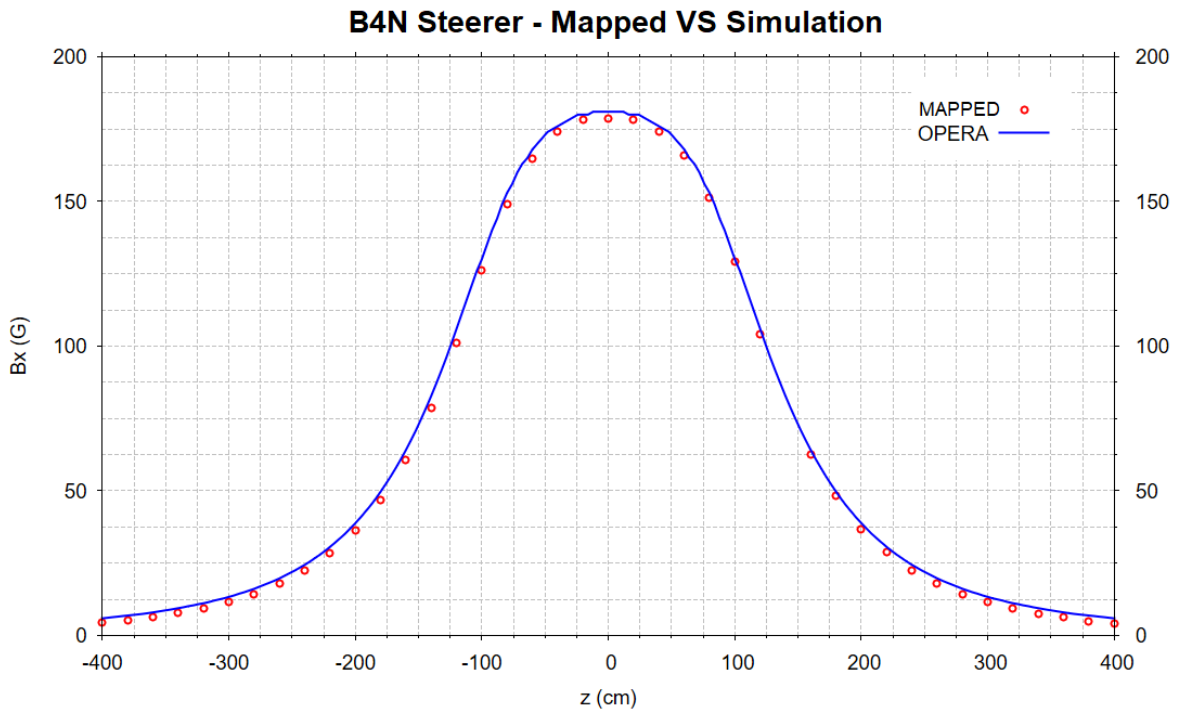

Figure 39 - Mapped VS Simulated Data for B4N Steerer

4.2 Set-up

To set-up a simulation in OPERA, first a SolidWorks model of the magnet was created, and the core exported as a .STEP file. The core was then imported into OPERA's 3D Modeller and magnet coils were added. The coils are simulated as single-turn inductors; thus, the current density was entered based on the area of the winding window. The B-H curve for J-Material was also added to the core properties. Air volumes were then added in stages to ensure a tight mesh on the area of interest and a full envelope of 500 x 500 x 500 mm. A 500 mm^3 envelope was decided upon to encompass the full area of the beamline and extremities of the magnetic fields. It was found that increasing the envelope beyond 500 mm drastically increased computational time with very little additional data. Finally, to decrease computational time, the model was trimmed to one-eighth since the magnet is symmetric about every axis. Figures 40 to 47 show these stages of set-up. Figure 48 shows a screenshot of the OPERA post-processor used to generate data reports. Generated contour and line plots are shown in Figures

49 and 50. Due to the computational time, approximately 1-2 hours for single magnets and two days for simulations involving both magnets, an optimization algorithm was not considered for this project.

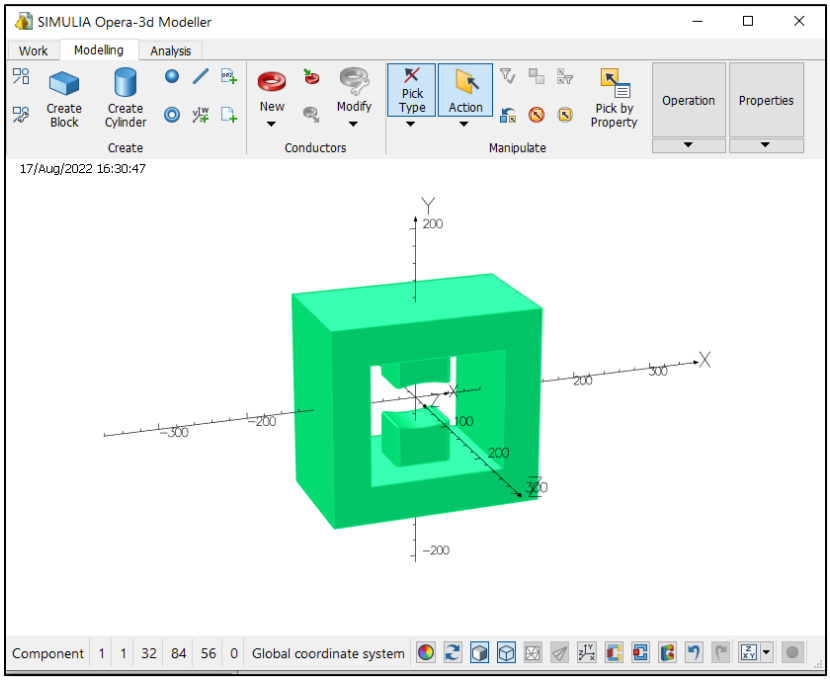

Figure 40 - OPERA Modeller with Imported .STEP File

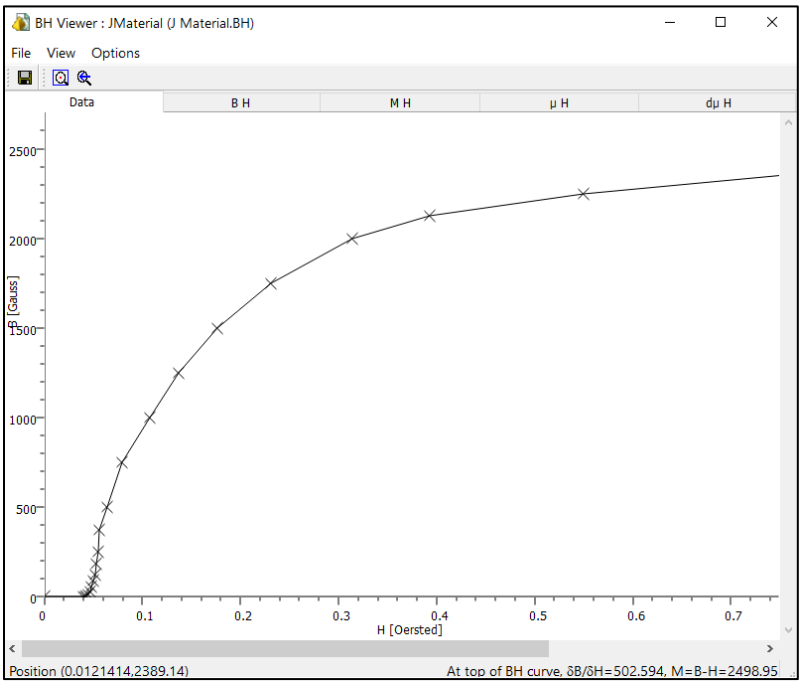

Figure 41 - OPERA BH Viewer Showing Imported J-Material B-H Data

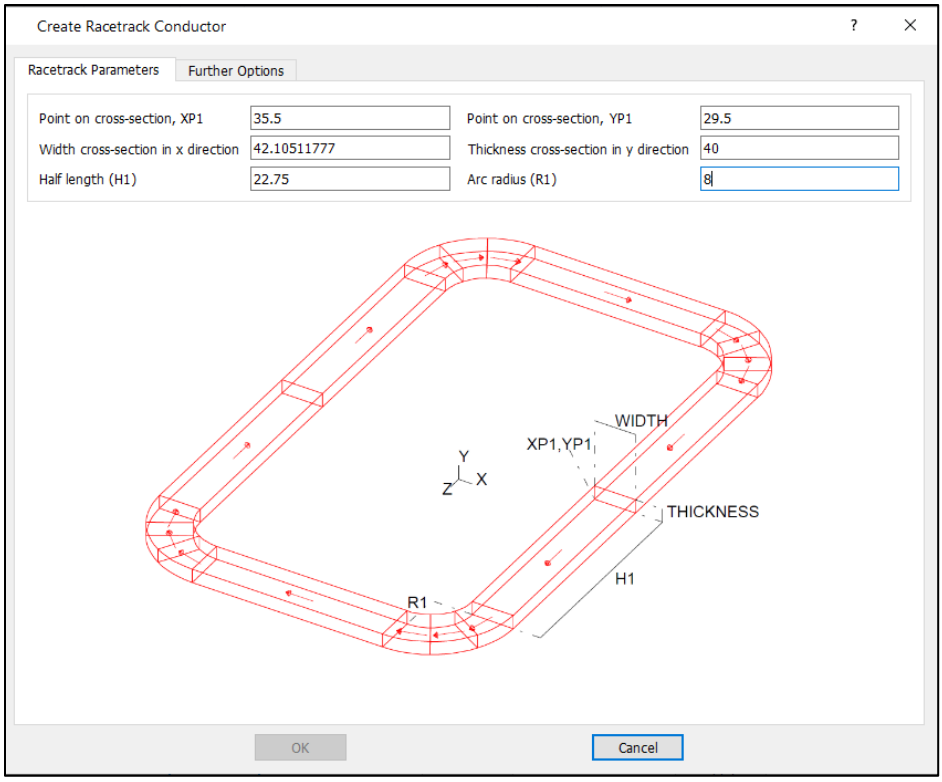

Figure 42 - OPERA Racetrack Creator Showing Conductor Size and Location Parameters

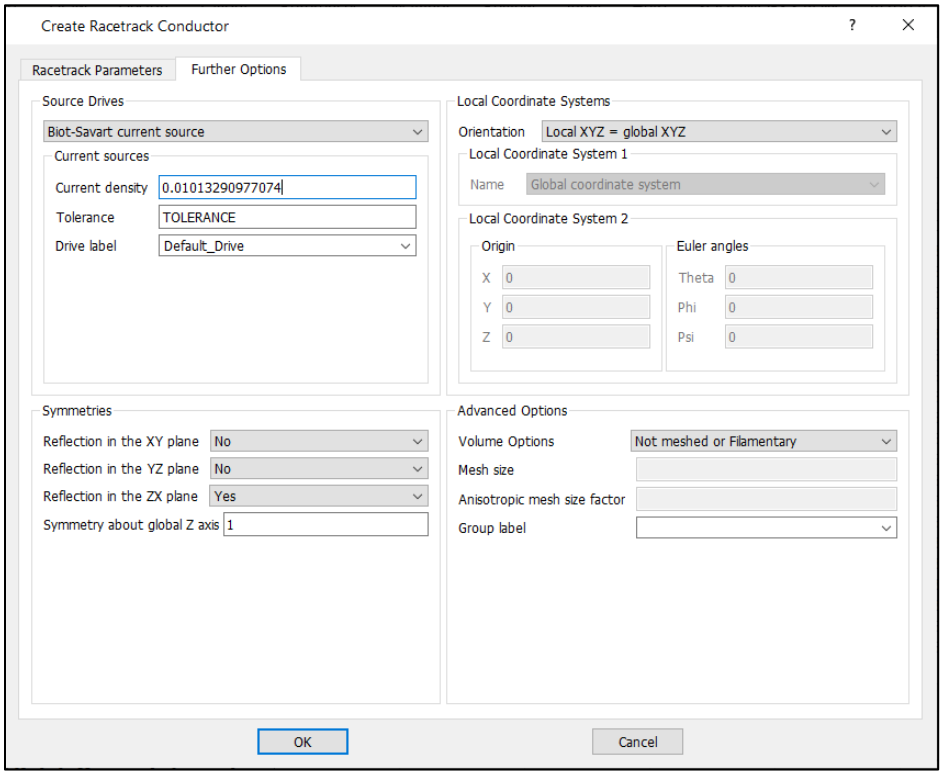

Figure 43 - OPERA Racetrack Creator Showing Conductor Electrical Parameters

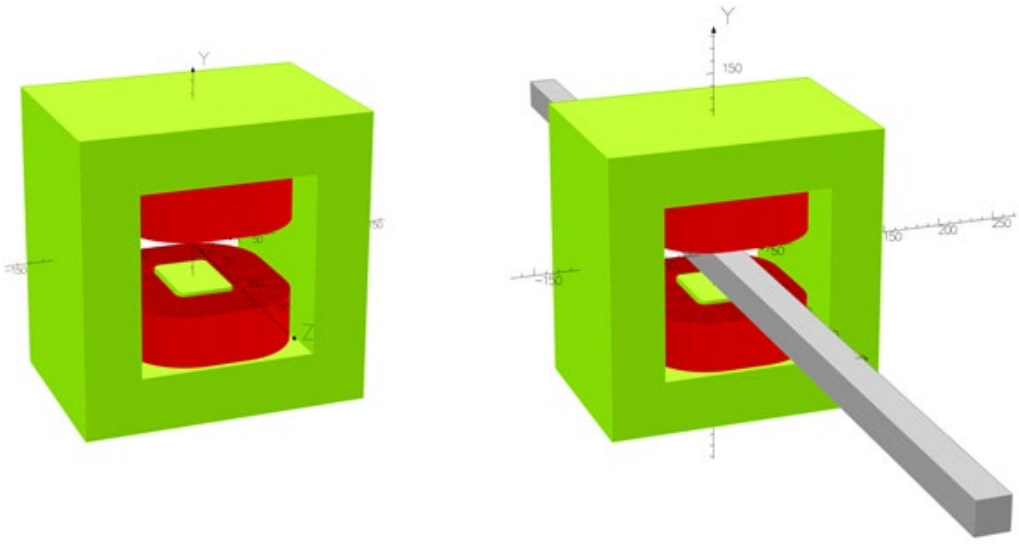

Figure 44 - Imported .STEP File with Single-Turn Inductors (Left) and Initial Air Volume in Area of Interest (Right)

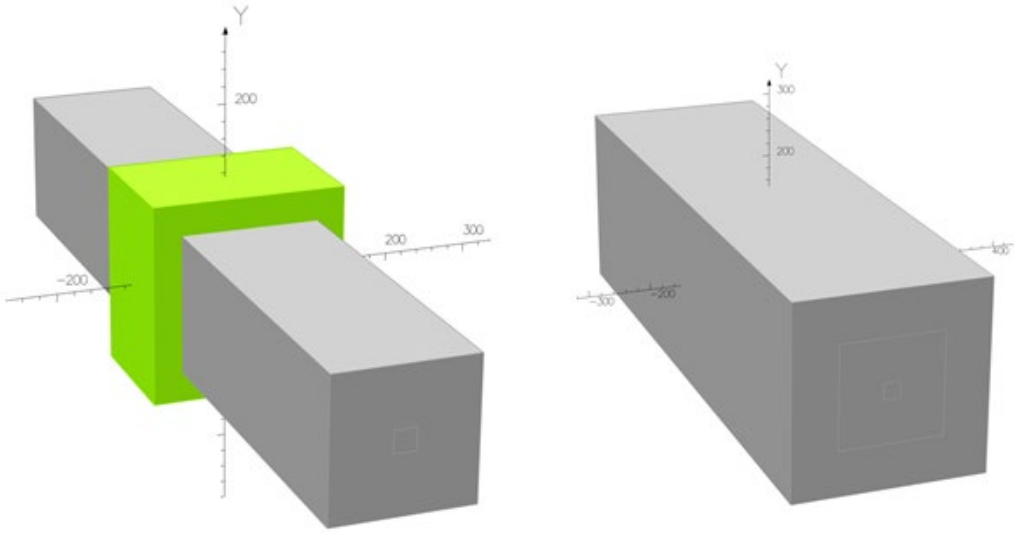

Figure 45 - Second (Left) and Third (Right) Air Volumes Added

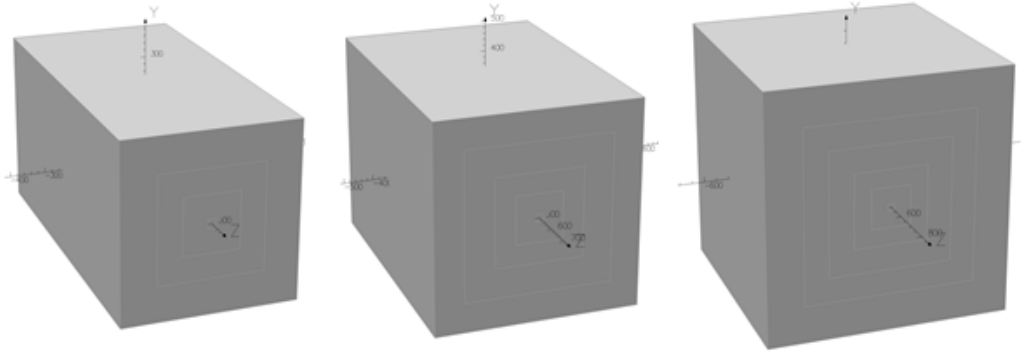

Figure 46 - Remaining Air Volumes Added for a 500 mm^3 Total Envelope

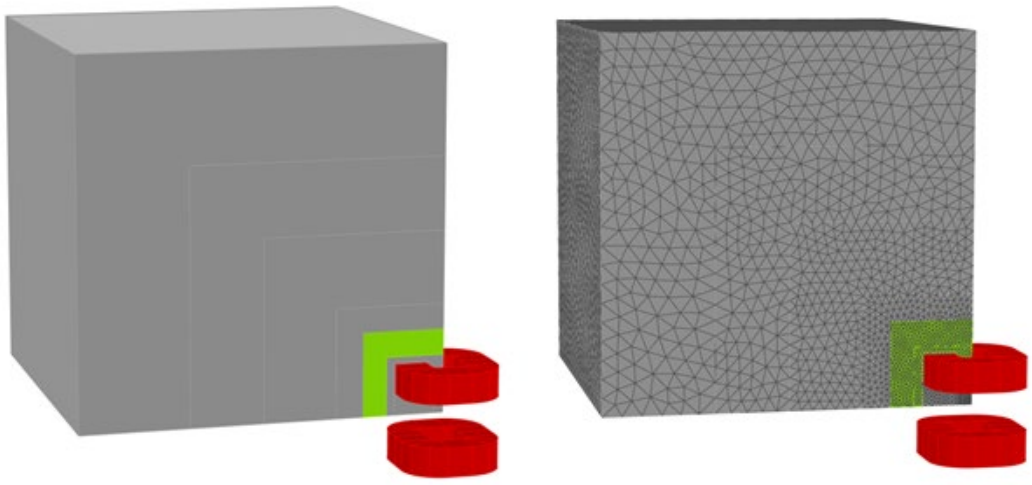

Figure 47 - Sectioned (Left) and Meshed (Right) Model

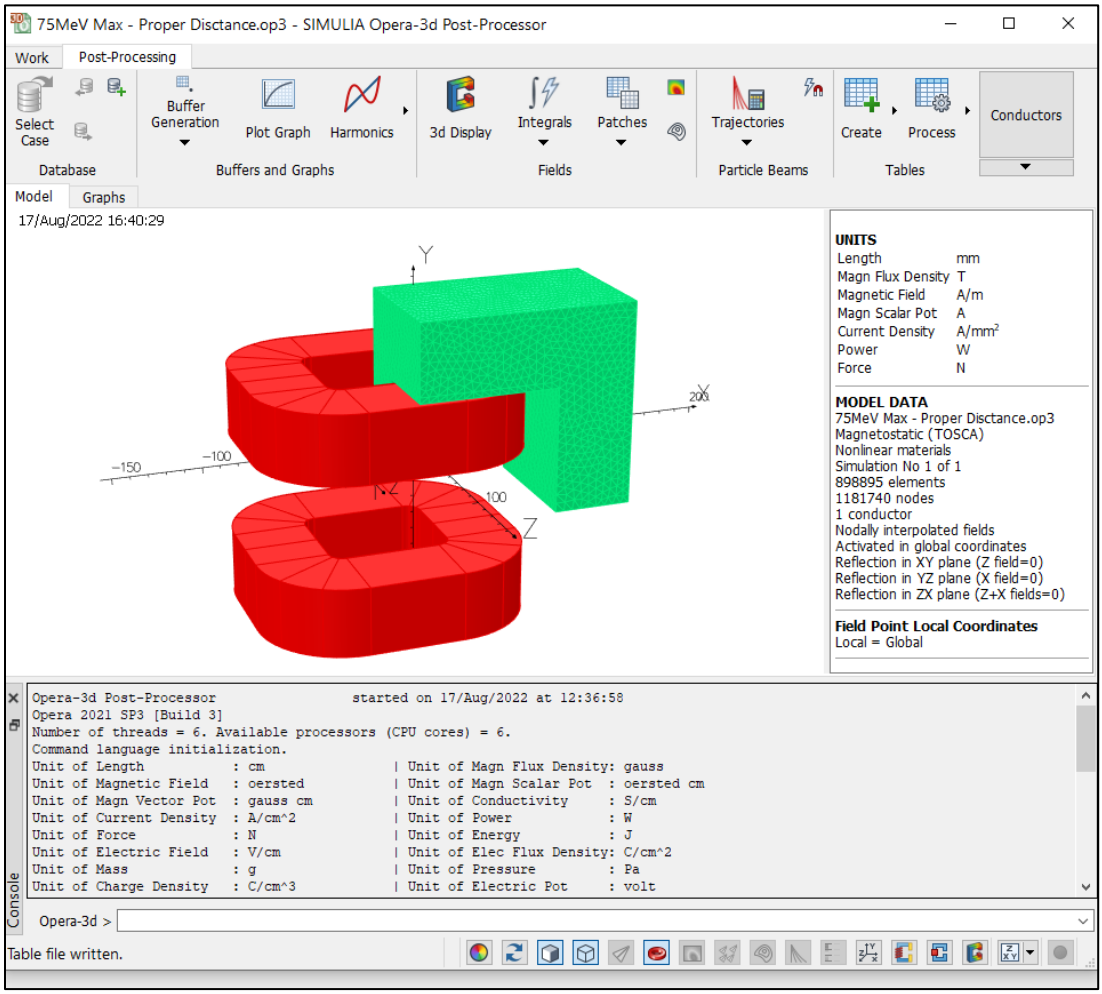

Figure 48 - OPERA Post-Processor Showing Completed Magnet Simulation

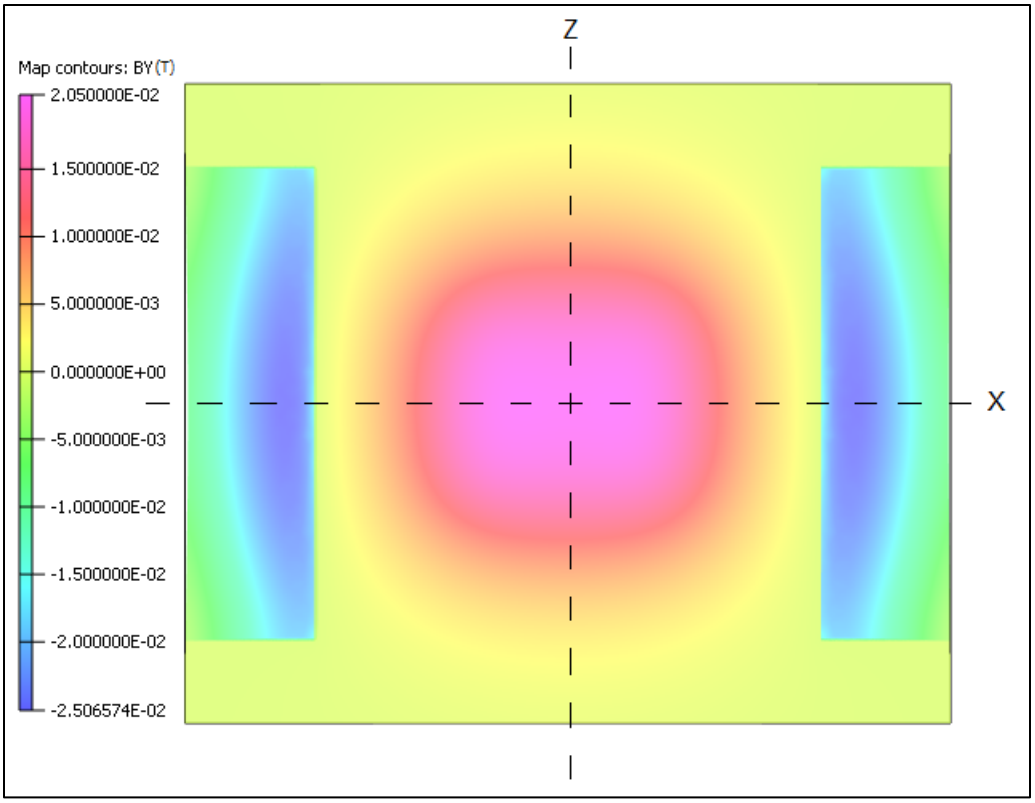

Figure 49 - Contour Plot Created with Post-Processor

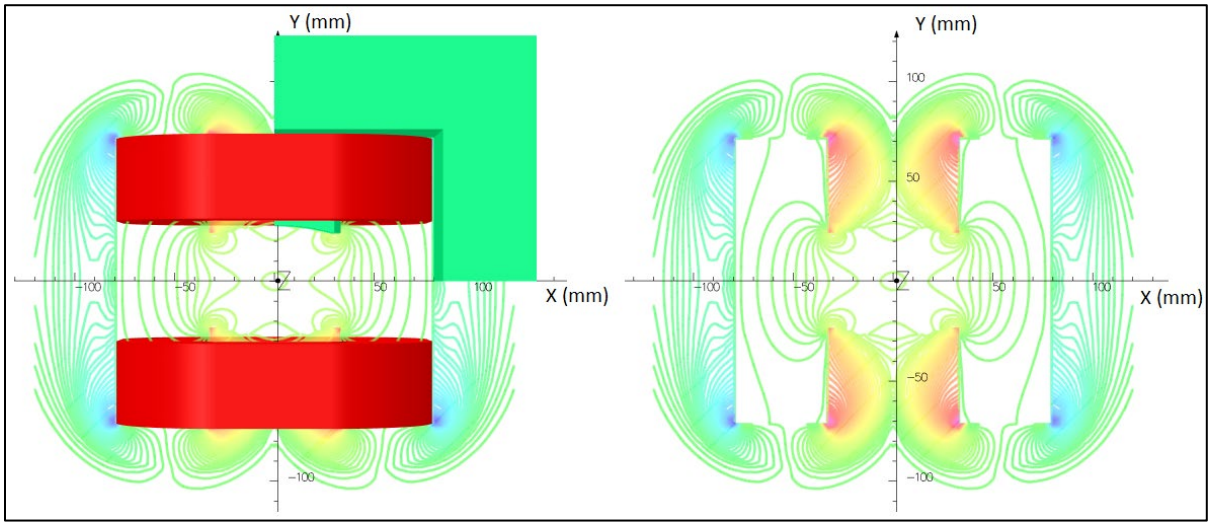

Figure 50 - Line Plot Created with Post-Processor
With Sectioned Model (Left) and Hidden Model (Right)

4.3 Magnetic Simulations

Throughout this project, there were many iterations of the final design and subsequently a plethora of simulations. Since it is impractical to show every simulation completed, only the first one, based on the original geometry, and the four final simulations are presented in this chapter.

4.3.1 Initial Simulations

The first simulation used the basic dimensions determined in Chapter 3. Figure 51 shows a graph of the field integrals in the area of interest with values in Tables 7 and 8. As expected, neither the magnetic field nor the integrated field match the required values.

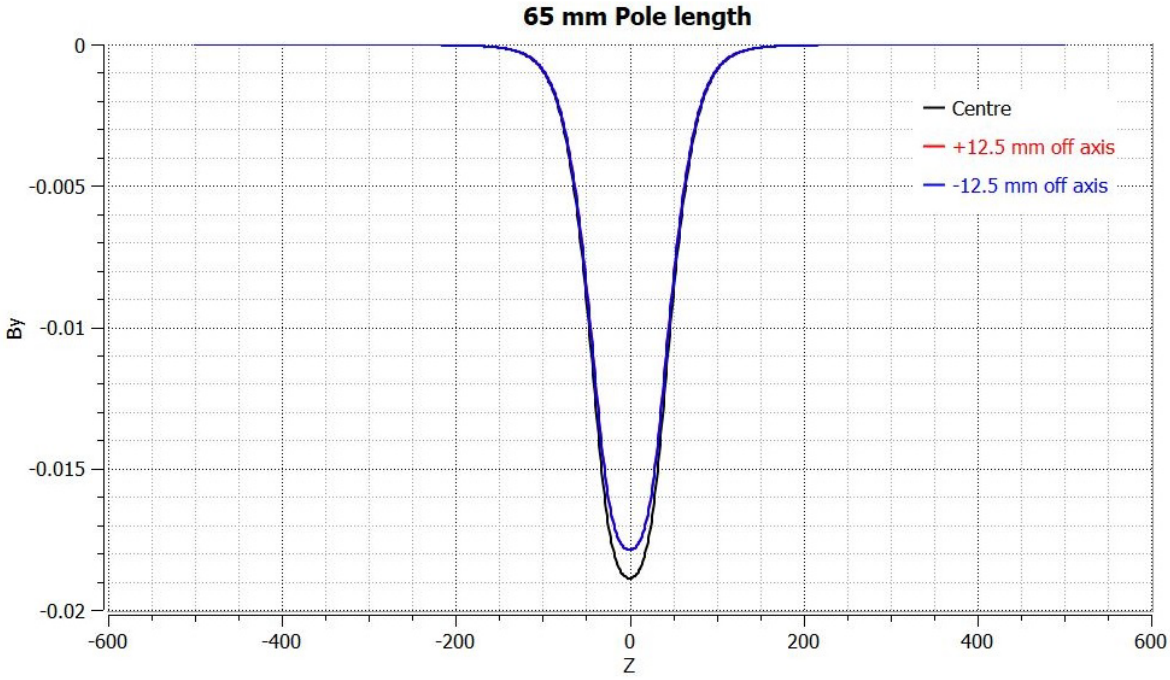

Figure 51 – Field Lines in Area of Interest - First Simulation

	Simulated Magnetic Field (T)	Calculated Magnetic Field (T)
Centre	0.018895	0.020354
+12.5 mm off axis	0.017888	0.020354
-12.5 mm off axis	0.017888	0.020354

Table 7 – Magnetic Field Values – Simulated VS Calculated – First Simulation

	Simulated Field Integral (Tm)	Calculated Field Integral (Tm)
Centre	0.00199665	0.00203545
+12.5 mm off axis	0.00188733	0.00203545
-12.5 mm off axis	0.00188733	0.00203545

Table 8 - Field Integral Values – Simulated VS Calculated – First Simulation

After the initial simulation, the pole length was iteratively changed from 65 mm to 55 mm, until the magnetic field, and integral, along the centre were relatively close to the required values. This resulted in an optimal pole length of 56.5 mm.

With the pole length determined, it was then necessary to alter the pole profile to increase field homogeneity in the area of interest. After many iterations, the pole profile was determined to be as shown in Figures 52 and 53. As seen in the preceding section, the concave profile essentially pushes the magnetic field towards the centre, creating a relatively homogenous field in the area of interest.

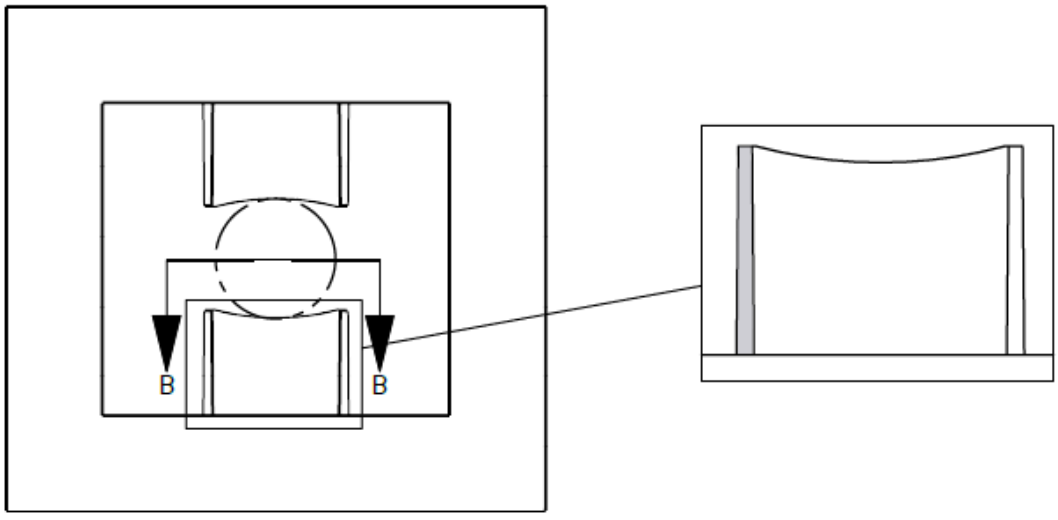

Figure 52 - Pole Profile - Front View (Left – Scale 1:4) & Front Cropped (Right – Scale 1:2)

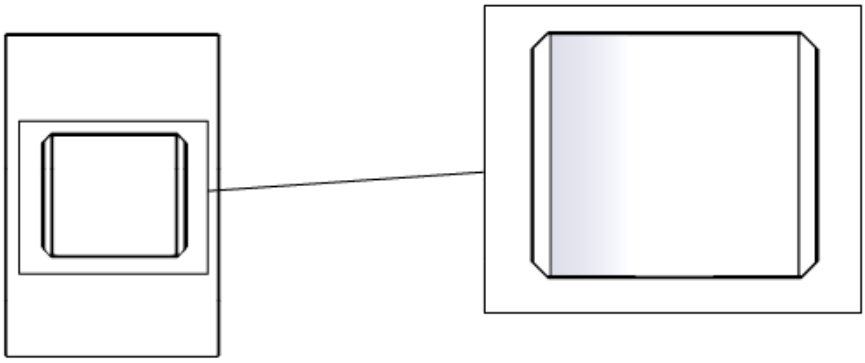

Figure 53 - Pole Profile – Section B-B (Left – Scale 1:4) and Cropped B-B (Right – Scale 1:2)

4.3.2 Final Simulations

Once the final dimensions were determined, a set of four simulations were completed to ensure compliance with requirement specifications *RS 2.3.1, RS 2.4.1 & RS 2.4.2*. These simulations are outlined below.

1. *75 MeV – 100 mm Raster Diameter – Single Magnet*

This simulation considers the magnet closest to the converter as it requires the *highest* magnetic field to deflect the beam to the *maximum* raster diameter. Table 9 shows the calculated values. An OPERA graph of the simulated field integrals can be seen in Figure 54 with the corresponding values in Table 10.

Calculated Values	
Magnetic Field (B)	0.020354542834 T
Integrated Field (Bρ)	0.002035454283 Tm

Table 9 - Single Magnet - 100mm Raster Diameter Calculated Values

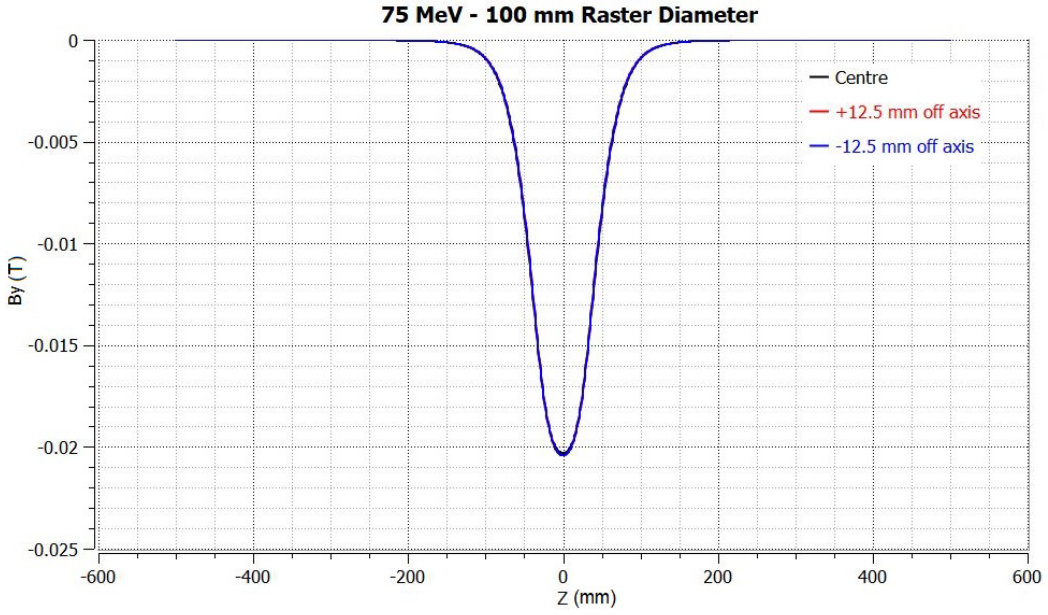

Figure 54 - Single Magnet - 100 mm Raster Diameter - Simulated Field Integrals

Figure 55 below shows the error of the magnetic field between the centre axis and +/-12.5 mm off axis. A maximum error of 0.308% can be seen as the field nears the centre of the magnet.

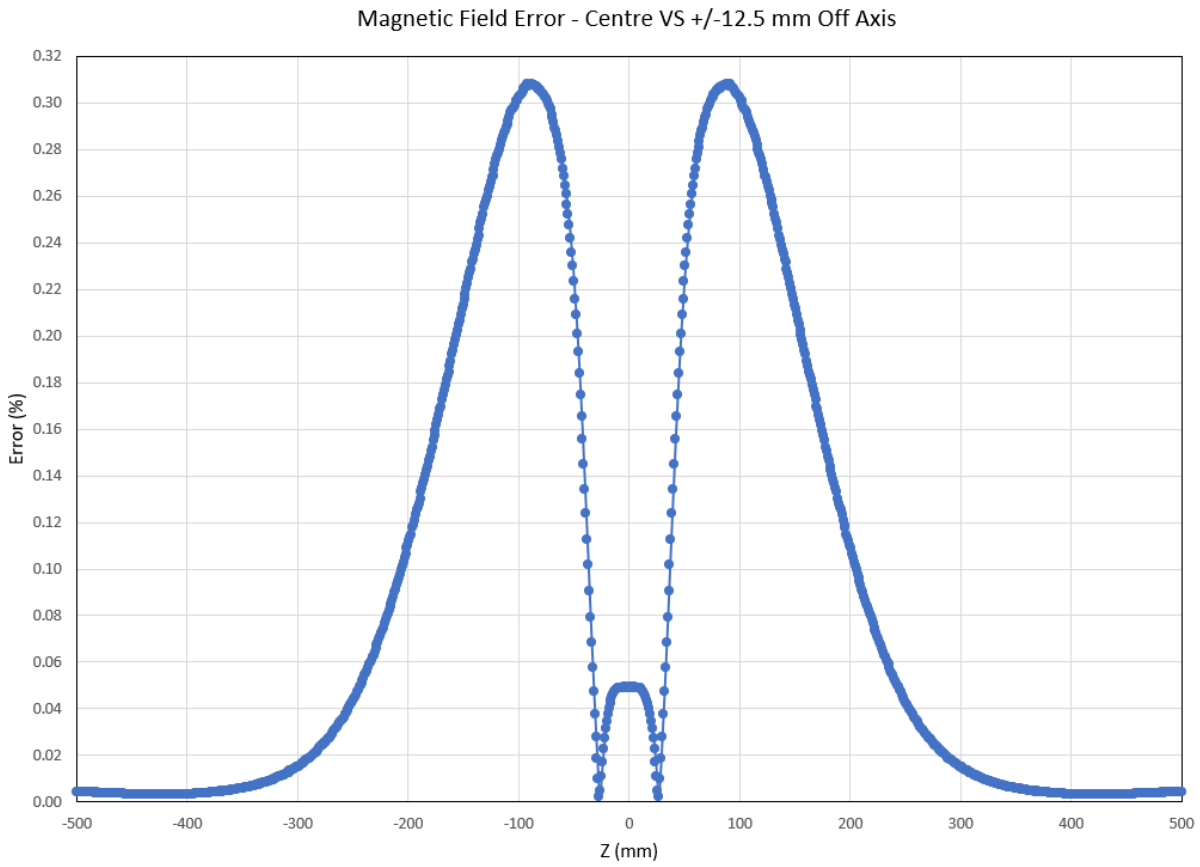

Figure 55 - Magnetic Field Error - Centre VS +/-12.5 mm Off Axis

Simulated Values	
Centre - Magnetic Field (B)	0.0203099 T
+/- 12.5 mm off axis - Magnetic Field (B)	0.0204098 T
Centre - Integrated Field (Bρ)	0.00204247 Tm
+/- 12.5 mm off axis - Integrated Field (Bρ)	0.00202946 Tm

Table 10 - Single Magnet - 100mm Raster Diameter Simulated Values

The results of this simulation show approximately 0.3% error between the calculated and simulated magnetic field values. Some small error is expected due to the inherent differences between calculations and computer simulations and is not concerning. This error will be accounted for during the mapping of the magnets by correlating applied current with measured magnetic field. The homogeneity of the field integral, in the area of interest shows an error of approximately 0.64%. The acceptability of this error was determined by considering the shape of the beam exiting the magnet and comparing it to the shape on the target. The maximum diameter of the electron beam passing through the raster system is expected to be 8 mm and must not have a deviation larger than 10% at the target [42]. Through geometrical analysis, using the simulated values, the maximum beam diameter at the target is 8.287 mm; approx. 3.4% deviation, well below the accepted 10%. Figure 56 shows a sketch of the geometrical analysis from SolidWorks, the yellow lines represent the beam trajectory in both the horizontal and vertical planes. The resultant beam shape is shown at 45°.

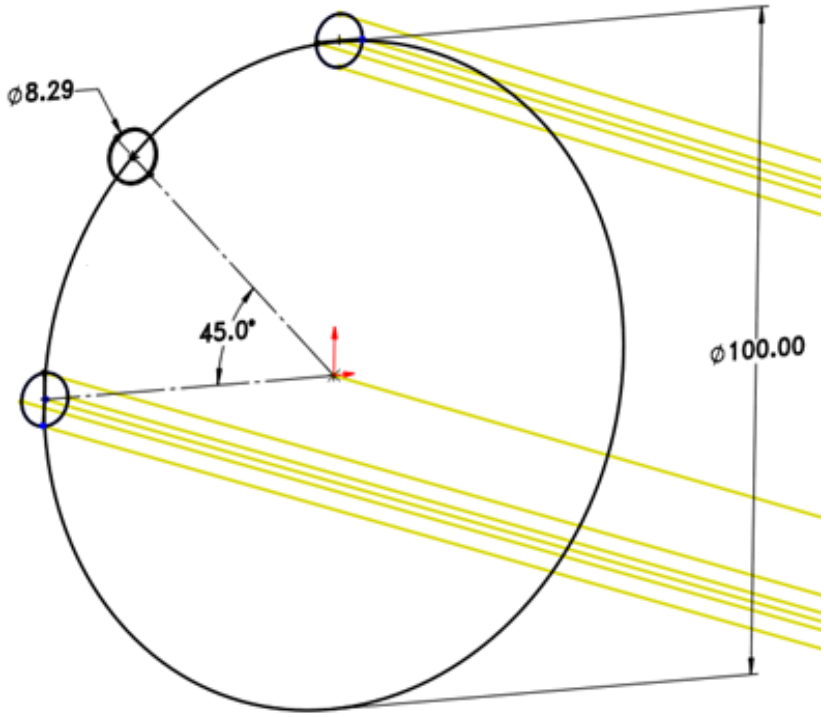

Figure 56 - Geometrical Analysis of Beam Shape with Maximum Error in Field Homogeneity

2. 75 MeV – 4 mm Raster Diameter – Single Magnet

This simulation considers the magnet furthest from the converter as it requires the *lowest* magnetic field to deflect the beam to the *minimum* raster diameter. Table 11 shows the calculated values. An OPERA graph of the simulated field integrals can be seen in Figure 57 with the corresponding values in Table 12.

Calculated Values	
Magnetic Field (B)	0.000779841286 T
Integrated Field (Bρ)	0.000077984129 Tm

Table 11 – Single Magnet - 4mm Raster Diameter Calculated Values

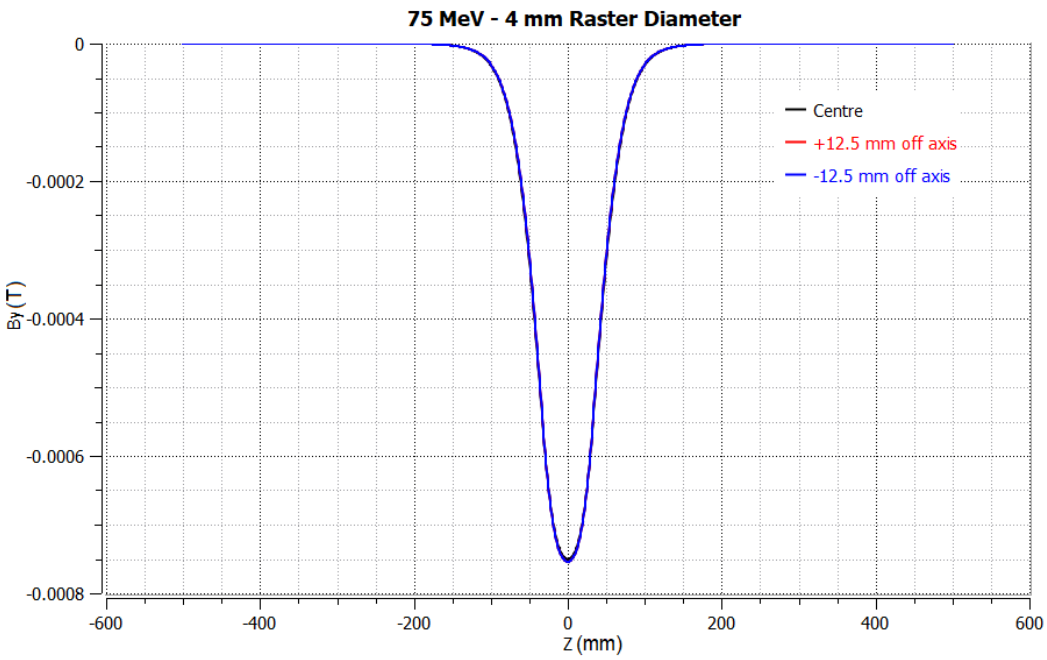

Figure 57 - Single Magnet - 4 mm Raster Diameter - Simulated Field Integrals

Simulated Values	
Centre - Magnetic Field (B)	0.000750436 T
+/- 12.5 mm off axis - Magnetic Field (B)	0.000754133 T
Centre - Integrated Field (Bρ)	0.0000745569 Tm
+/- 12.5 mm off axis - Integrated Field (Bρ)	0.0000740768 Tm

Table 12 - Single Magnet - 4mm Raster Diameter Simulated Values

Although the simulated values are slightly lower than calculated, this simulation shows a homogeneous magnetic field and integral, with the same 0.64% error seen in the simulation above. Again, the small error in the magnitude of the magnet field will be mitigated during mapping of the magnet and the field error, as stated in the previous simulation, is acceptable. Figure 58 below shows the dominant pole profile dimensions X.XX and Y.YY in which a small deviation from the optimal values causes a discrepancy between central and +/-12.5 mm off axis magnetic fields. The effects of changing these values can be seen in Figures 59 and 60 where a deviation of 1 mm was applied from the optimal values.

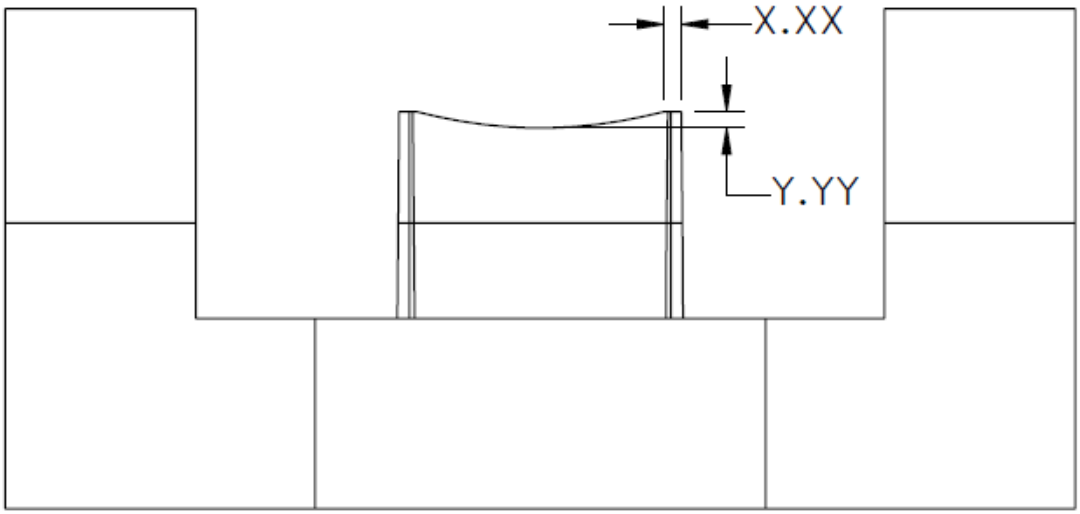

Figure 58 - Half Core Showing Dominant Profile Dimensions (Scale 1:2)

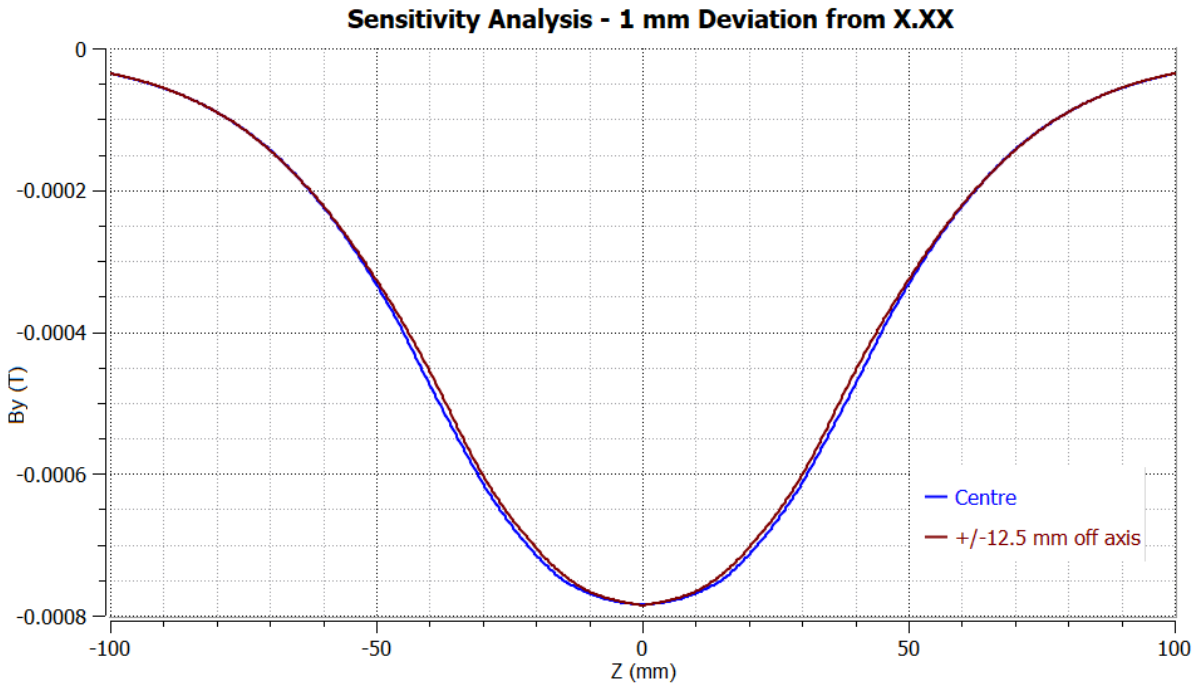

Figure 59 - 1 mm Deviation from Optimal Value of X.XX
(Magnified to Area of Greatest Error)

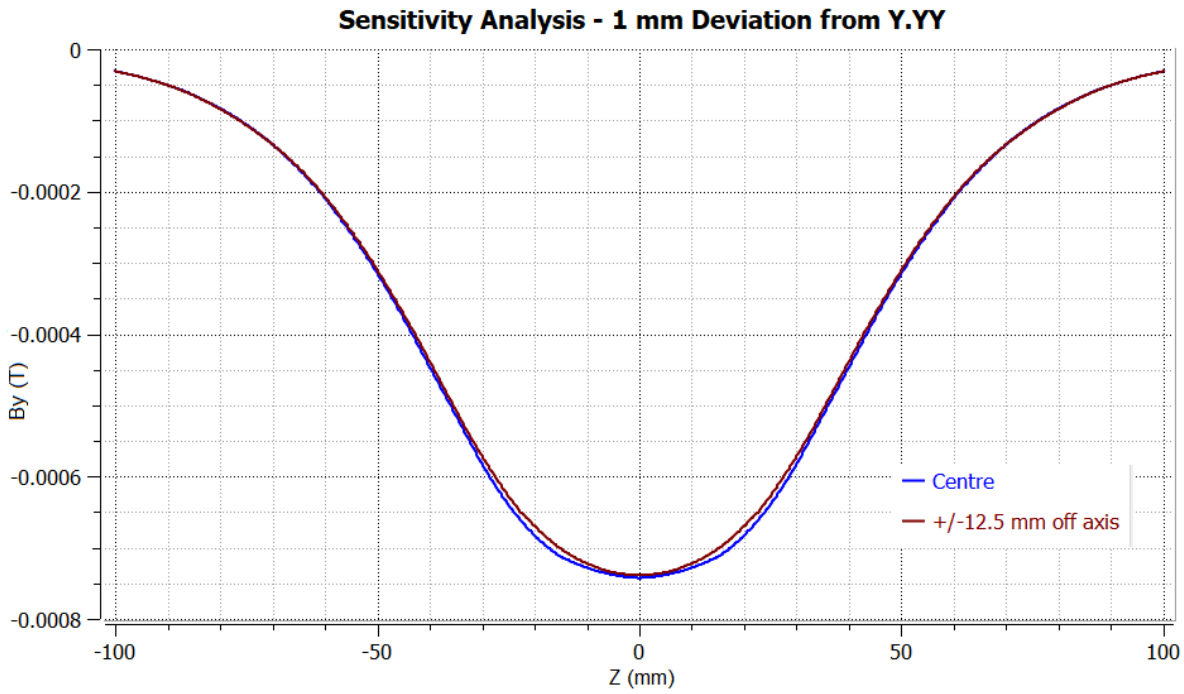

Figure 60 -1 mm Deviation from Optimal Value of Y.YY
(Magnified to Area of Greatest Error)

3. 75 MeV – 100 mm Raster Diameter – Both Magnets

This simulation considers both magnets deflecting the beam at the *maximum* raster diameter. Table 13 shows the calculated values. An OPERA graph of the simulated field integrals can be seen in Figure 61 with the corresponding values in Table 14.

Calculated Values		
Magnet 1	Magnetic Field (B)	0.019495451357 T
	Integrated Field (Bρ)	0.001949545135 Tm
Magnet 2	Magnetic Field (B)	0.020354542834 T
	Integrated Field (Bρ)	0.002035454283 Tm

Table 13 - Both Magnet - 100mm Raster Diameter Calculated Values

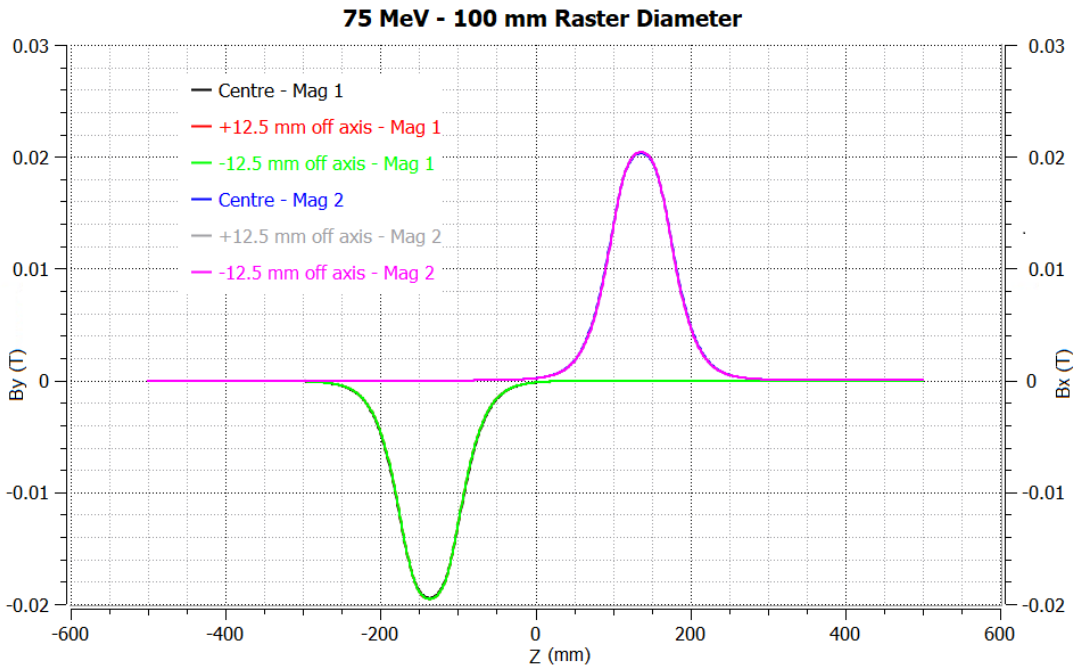

Figure 61 - Both Magnets - 100 mm Raster Diameter - Simulated Field Integrals

Simulated Values		
Magnet 1	Centre - Magnetic Field (B)	0.0195602 T
	+/- 12.5 mm off axis - Magnetic Field (B)	0.0195459 T
	Centre - Integrated Field (Bρ)	0.00195277 Tm
	+/- 12.5 mm off axis - Integrated Field	0.00194030 Tm
Magnet 2	Centre - Magnetic Field (B)	0.0203085 T
	+/- 12.5 mm off axis - Magnetic Field (B)	0.0204084 T
	Centre - Integrated Field (Bρ)	0.00203915 Tm
	+/- 12.5 mm off axis - Integrated Field	0.00202611 Tm

Table 14 - Both Magnets - 100mm Raster Diameter Simulated Values

The results of the dual magnet simulation above confirm the results seen in the individual magnet simulations. There are no unexpected issues when both magnets are in operation.

4. 75 MeV – 4 mm Raster Diameter – Both Magnets

This simulation considers both magnets deflecting the beam at the *minimum* raster diameter. Table 15 shows the calculated values. An OPERA graph of the simulated field integrals can be seen in Figure 62 with the corresponding values in Table 16.

Calculated Values		
Magnet 1	Magnetic Field (B)	0.000779841286 T
	Integrated Field (Bρ)	0.000077984129 Tm
Magnet 2	Magnetic Field (B)	0.000814208148 T
	Integrated Field (Bρ)	0.000081420814 Tm

Table 15 - Both Magnet - 4mm Raster Diameter Calculated Values

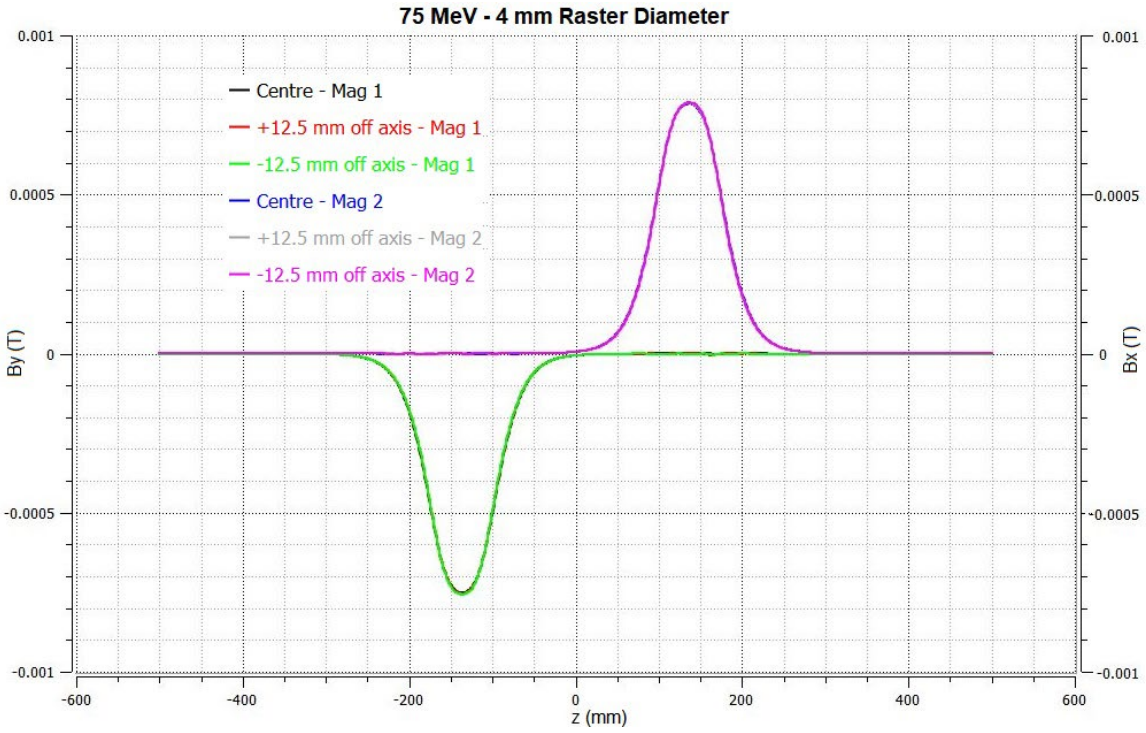

Figure 62 - Both Magnets - 4 mm Raster Diameter - Simulated Field Integrals

Simulated Values		
Magnet 1	Centre - Magnetic Field (B)	0.000785668 T
	+/- 12.5 mm off axis - Magnetic Field (B)	0.000755651 T
	Centre - Integrated Field (Bρ)	0.0000747724 Tm
	+/- 12.5 mm off axis - Integrated Field	0.0000755651 Tm
Magnet 2	Centre - Magnetic Field (B)	0.000785668 T
	+/- 12.5 mm off axis - Magnetic Field (B)	0.000788780 T
	Centre - Integrated Field (Bρ)	0.000078284 Tm
	+/- 12.5 mm off axis - Integrated Field	0.000077301 Tm

Table 16 - Both Magnets - 4mm Raster Diameter Simulated Values

The simulations above, involving both magnets, re-iterate what was seen in the single magnet simulations. With the same approximate errors and no noticeable negative effects due to the interaction between the two magnets, these simulations show a successful magnet design.

Chapter 5 – Magnet Electrical Properties

This chapter outlines the process to determine the relevant electrical properties of the magnets to be used in power supply development at TRIUMF. A table of tabulated values can be seen at the end of this chapter

1. Coil Resistance

It is important to understand the resistance of the magnet coils as it directly relates to power supply development. With litz wire, the DC resistance is calculated using Equation 20 [25]

$$R_{LW_{max}} = \frac{R_{sw_{max}}}{n_{sw}} * k_{n_b} * k_{BW} \tag{20}$$

where $R_{LW_{nom}}$ is the nominal resistance value of a single wire, n_{sw} the number of single wires and k_{BW}=1.03 the factor for broken wires.[16] k_{n_b} is a factor of shortening of length due to the bunching process and is calculated as follows [25].

$$k_{n_b} = 1 + \sum_{i=1}^{n_b} 0.02 = 1 + \sum_{i=1}^{2} 0.02 = 1.04 \tag{21}$$

Using the value obtained from Equation 21, the maximum DC resistance is as follows.

$$R_{LW_{max}} = \frac{3.7795\ \Omega/m}{400} * 1.04 * 1.03 = 0.010121501\ \Omega/m$$

Since the magnets will be operated with AC current, the AC resistance must be calculated as it will be slightly higher than at DC. By considering the ratio of AC to DC resistance the final AC resistance value can be calculated using Equation 22 [25], where *H* is the resistance ratio of individual strands (1 for 0-350 kHz), *K,* a constant depending on *N* (2 for any number of strands above 27), D_i the diameter of the individual strands, D_o the

[16] Due to the small diameter of litz wires it is possible that some wires will break during construction.

diameter of the finished cable, and G the eddy current basis factor, calculated using Equation 23 [25].

$$\frac{R_{AC}}{R_{DC}} = H + K\left(\frac{N * D_i}{D_o}\right)^2 * G \tag{22}$$

$$G = \left(\frac{D_i\sqrt{F}}{10.44}\right)^2 \tag{23}$$

$$G = \left(\frac{(0.0031\ in) * \sqrt{100{,}000\ Hz}}{10.44}\right)^4 = 7.774 * 10^{-5}$$

$$\frac{R_{AC}}{R_{DC}} = 1 + 2\left(\frac{400 * 0.0061\ in}{0.15748\ in}\right)^2 * 7.774 * 10^{-5} = 1.03733$$

With the calculated ratio, the AC resistance was calculated considering the DC resistance as follows.

$$R_{AC} = 1.03733 R_{DC} = (1.03733) * \left(0.010121501\ {}^{\Omega}/_{m}\right) = 0.010499\ {}^{\Omega}/_{m}$$

The total length of wire in the coils was determined to be approx. 82 m, therefore the total AC resistance per magnet is 0.860918 Ω.

2. Current

The current is easily calculated by considering the worst-case MMF and the number of turns per magnet.

$$I = \frac{MMF}{\#\ of\ turns} = \frac{890.8692\ A - turns}{228\ turns} = 3.977096875\ A \approx 4\ \text{A}$$

3. Voltage Drop

With the current and total resistance known, the voltage drop was calculated as follows.

$$V = IR = 4\ A * 0.860918\ \Omega = 3.443672\ \text{V} \approx 3.5\ \text{V}$$

4. Inductance

Inductance is very difficult to calculate analytically and is typically determined by field measurements. Fortunately, the inductance can be estimated by considering the stored energy in the magnet; a value that can be extracted from the OPERA simulations. For the worst-case (75 MeV & 100 mm raster diameter), the stored energy was 0.0110853 J. Equation 24 shows the relationship between stored energy and inductance (*L*).

$$Stored\ Energy = \frac{1}{2}LI^2 \tag{24}$$

Rearranging Equation 24 to solve for inductance leads to Equation 25

$$L = \frac{2 * Stored\ Energy}{I^2} \tag{25}$$

$$L = \frac{2 * (0.0110853\ J)}{(4\ A)^2} = 0.0014\ H$$

5. Voltage Spike due to Fast Switching

AC circuits are susceptible to voltage spikes proportional to the operating frequency, as such, this must be considered during power supply development. Equation 26 shows this relationship.

$$V_{spike} = L\frac{di}{dt} \tag{26}$$

Using the inductance calculated above, maximum current of 4 A and frequency of 10 kHz, the voltage spike was calculated as follows.

$$V_{spike} = (0.0014\ H) * \frac{8\ A}{0.0001\ s} = 112\ V$$

6. *Tabulated Magnet Electrical Properties*

Table 17 outlines the relevant electrical properties for a single magnet

Magnet Electrical Properties – Single Magnet	
Max Electron Beam Energy	75 MeV
Max Magnetic Field	0.0205 T (205 G)
Current	4 A
Voltage	3.5 V
Inductance	0.0014 H
Max Frequency	100 kHz
Voltage Spike @ 100 kHz	112 V

Table 17 – Tabulated Magnet Electrical Properties

Chapter 6 – Summary of Results

The work presented in this thesis outlines the successful design of a new AC raster system to be implemented into the new ARIEL Electron Target beamline at TRIUMF. These magnets have been designed using the latest technologies available, including specially insulated litz wire for the conductors, radiation resistant 3D printable PPS for the coil bobbins, J-Material ferrite for the core and a phenolic G11 exterior shell. Combined with the metalized ceramic beam tube, this system meets all requirements outlined in Chapter 2. Table 18 shows a compliance matrix ensuring all requirements are met.

Requirement Specification	Description	Met
RS 2.1.1	Lifetime radiation of 2.31×10^5 Gy	Yes
RS 2.2.1	Minimum distance of 5.2 m from target	Yes
RS 2.2.2	Integration into existing beamline	Yes
RS 2.3.1	Compatible with 75 MeV electron beam	Yes
RS 2.3.2	Compatible with beam size of Ø25 mm	Yes
RS 2.4.1	Largest scanned area of Ø100 mm	Yes
RS 2.4.2	Smallest scanned area of Ø4 mm	Yes
RS 2.4.3	Independent rastering in vertical and horizontal	Yes
RS 2.4.4	Compatible with a frequency of 10 kHz	Yes
RS 2.4.5	It should be possible to irradiate any shape.	Yes

Table 18 – Requirements Compliance Matrix

The design specifications determined in Chapter 3 were applied to simulations using Dassault Systèmes OPERA 3D and iterated until the magnetic properties were optimized about the area of interest; Ø25 mm as per *RS 2.3.2* Five of these simulations, based on the minimum and maximum requirements, were presented in Chapter 4. The output variables of these show the induced magnetic field and the value of the field integrals along the axis of the beamline.

The first simulation applied the basic dimensions from Chapter 3 along with a flat pole profile as a baseline. It showed a large error with respect to the calculated values and non-homogenous field integrals about the area of interest. This basic design was the starting point for iterations that led to the concave pole profile and a pole length of 56.5 mm. The subsequent simulations presented were completed to ensure an accurate design.

The first, of the four final simulations, considered the magnet closest to the target, which requires the highest magnetic field at the maximum raster diameter of 100 mm. This simulation showed less than 0.3 % difference between the calculated and simulated magnetic field values. This small error is expected when comparing computational results to theoretical values and is not concerning.

The second simulation considered the magnet furthest away from the target as it will require the smallest magnetic field at the smallest raster diameter of 4 mm. The error between the calculated and simulated values was slightly higher at 3% for this small magnetic field but again is not concerning. Once the magnets have been manufactured, they will be mapped at TRIUMF and a B-I graph will be created. This correlates the supplied current with the induced magnetic field and thus allows for tuning of the raster system.

The homogeneity of the field integrals, +/-12.5 mm off axis, showed, in both cases, an error of only 0.63% with respect to the centre integral. This error was deemed acceptable by comparing the shape of the beam leaving the magnets to the shape at the target. A maximum deviation of approx. 3.5% from the original shape was found and is well below the specified maximum of 10% deviation.

The next set of simulations considered the real-world application of both magnets working in-tandem to ensure there were no unexpected issues. The results of these simulations echoed the

findings in the individual simulations and showed a successful working raster system at both the maximum and minimum requirements.

Chapter 7 - Discussion

The ARIEL facility, in development at TRIUMF, will contain a new electron target irradiation module complete with a state-of-the-art target design. This new target design is susceptible to destruction by instantaneous spot heating of the electron beam. To mitigate this issue, a set of AC raster magnets, working in tandem, are required to raster the beam at 10 kHz. The aim of this project was to contribute to the world of accelerator magnets by creating a high frequency raster system that utilizes advanced conductor, core, and material technologies.

Most of the requirements that were gathered from released TRIUMF design notes were easily interpreted, except for *RS 2.4.5* which stated the desire to raster any pattern. This is not practical as the waveform is directly related to the complexity of the pattern and requires higher harmonics. To quantify this, a study was completed on potential patterns and waveforms, and a design frequency of 100 kHz was decided upon. This allows for a fundamental frequency of 10 kHz with 9 harmonics, much higher than the typical 3 harmonics seen at other labs around the world.

The main challenge to overcome with this system was the effects of eddy currents caused by fast switching of the AC current. Eddy currents cause the skin effect which concentrates the current to the outside of the conductor, creating increased resistance, heat, and the inability to quickly change the polarity of the magnetic field. This issue can be eliminated, in the conductor, by choosing a diameter smaller than the skin depth at the highest frequency and led to the choice of litz wire.

Litz wire, short for the German word, litzendraht, meaning woven wire, is comprised of many small wires individually insulated and twisted together. This allows for the individual wires to

be smaller than the skin depth without sacrificing the overall cross-section of the conductor. For this application, litz wire consisting of 400 strands of 0.08 mm diameter wires was chosen with a bunching method consisting of 5 twisted bunches of 16 wires, creating 5 bunches of 80 that are then twisted together. Insulated with ETFE, this litz wire also meets the radiation requirement of $2.3x10^5$ Gy. Since there are no other insulating requirements, the litz wire can be coiled directly onto bobbins to be assembled onto the electromagnets. A new 3D printable material, PPS, will be used to manufacture the bobbins as it also meets the radiation requirements.

Magnet cores are also susceptible to issues with respect to eddy currents and thus the standard solid steel core design could not be used. At low frequencies, magnet cores are comprised of thin laminated sheets of steel smaller than the skin depth, but at high frequencies, this becomes impractical. A sheet size of less than 0.02 mm would be required for this application. A solution was found in ferrite, an amorphous material comprised of iron-oxide crystals and other metals smaller than the skin depth. Typically used in transformers, Magnetics supplies a J-Material ferrite that meets the requirements for this application. Manufactured in small blocks, several of these will be epoxied together and machined to match the designed core profile.

With the basic design of the raster magnets determined, simulations could be completed to optimize the pole profile and create a homogenous magnetic field within the 25 mm area of interest. After many iterations, a concave pole with a length of 56.5 mm showed the optimum results. An error of less than 1% was found in the field homogeneity for both the maximum and minimum raster diameters with a slightly higher error found between the magnetic field values at the smallest raster diameter. Once the magnets have been manufactured, they will be

mapped at TRIUMF and a magnetic field vs current (B-I) will be created. This means the small error of the magnetic field at the low end will be compensated for.

The final component of this raster system is the beampipe which again is susceptible to eddy currents and thus cannot be metallic. A metallic beampipe smaller than the skin depth would implode once the vacuum was applied to the beamline. A ceramic beampipe made from Kyocera's FRIALIT F99.7 was chosen to mitigate any eddy current issues. Unfortunately, since the ceramic is non-conductive, the electron beam will deposit electrical charges on the inner surface causing a deflection of the beam and ultimately large discharges. This means a conductive coating must be applied to the inner surface of the ceramic smaller than the skin depth. For this application, either nickel or titanium will be used depending on manufacturer preference. A DN 50 CF flange will also be brazed onto each end to integrate with the existing beamline.

As shown in Table 18, this raster system meets all requirements set forth by the ARIEL project at TRIUMF by utilizing the latest technologies in materials, components, and manufacturing processes.

- Specially insulated litz wire for the conductors
- Radiation resistant 3D printable PPS for the coil bobbins
- J-Material ferrite for the magnet cores
- Phenolic glass-laminate thermoset – G11 for the outer casing
- Metalized ceramic beampipe

The main limitation for this system is the inability to create patterns that require more than 9 harmonics above the fundamental frequency.

Chapter 8 – Conclusions

8.1 Conclusion

This work presented a solution to the raster system requirements for the ARIEL electron target station at TRIUMF. Two AC magnets will be used in tandem to allow the electron beam to be rastered at a frequency of 10 kHz. This project initially looked at raster systems throughout the world and found that only a concept for proton rastering at the European Spallation Source followed a similar approach. The design outlined in this report takes advantage of new technologies to create an advanced raster system never before seen.

8.2 Future Work

The ARIEL project is expected to be completed in summer 2026, as such, there is still a substantial amount of development to be completed. Since these magnets will be a part of the ARIEL electron target beamline at TRIUMF, it is unlikely this raster system will be installed before 2024. The final design note is expected to be completed by the end of 2022 with procurement and manufacturing beginning in early 2023. Completed magnet assemblies are expected for bench testing in late to early 2023-2024.

The main outstanding item, currently in development, is the power supply system, which can now be completed using the values specified in this thesis. The remaining tasks to be completed are as follows:

- Complete detail design and create a set of manufacturing drawings
- Manufacture, assemble and bench test
    - Map magnets and create B-I curves
- Integration into the control system EPICS

- Installation into beamline
- Commissioning of complete system

The current timeline anticipates these tasks to be completed by June 2026.

Appendix A

Typical Properties of Tefzel™ ETFE

Property*	ASTM Method	Unit	Tefzel™ ETFE
Mechanical			
Melt Flow Rate	D3159	g/10 min	7
Ultimate Tensile Strength, 23 °C (73 °F)	D638	MPa (psi)	46 (6,500)
Ultimate Elongation, 23 °C (73 °F)*	D638	%	300
Compressive Strength, 23 °C (73 °F)**	D695	MPa (psi)	17 (2,500)
Flexural Modulus	D790	MPa (psi)	600–1,200 (85,000–170,000)
Impact Strength, 23 °C (73 °F)	D256	J/m (ft·lb/in)	No Break
Hardness, Durometer, Shore D	D2240		67
Coefficient of Friction, Metal/Film	D1894		0.23
Deformation Under Load, 23 °C (73 °F), 1,000 psi, 24 hr	D621	%	0.3
Linear Coefficient of Expansion	E831	mm/mm· °Cx10^{-5} (in/in· °Fx10^{-5})	
0–100 °C (32–212 °F)			13.1 (7.3)
100–150 °C (212–302 °F)			18.5 (10.3)
150–200 °C (302–392 °F)			25.2 (14)
Specific Gravity	D792		1.71
Water Absorption, 24 hr	D570	%	0.007
Electrical			
Surface Resistivity	D257	ohm·sq	>10^{16}
Volume Resistivity	D257	ohm·cm	>10^{16}
Dielectric Strength, 23 °C (73 °F)	D149	kV/mm (V/mil)	
0.25 mm (10 mil)			64 (1,600)
3.20 mm (126 mil)			15 (370)
Dielectric Constant, 22 °C (72 °F), 1 MHz	D1531		2.6
Dissipation Factor, 22 °C (72 °F), 1 MHz	D1531		0.007
Arc Resistance	D495	sec	122
Thermal			
Melting Point	DTA D3418	°C (°F)	220–280 (428–536)
Heat of Fusion	DSC D3417	kJ/kg (Btu/lb)	50.7 (21.8)
Specific Heat	DSC	kJ/kg·K (cal/g·°C)	
25 °C (77 °F)			0.25
100 °C (212 °F)			0.3
150 °C (302 °F)			0.34
300 °C (572 °F) (Melt)			0.38
Heat of Combustion	D240	MJ/kg (Btu/lb)	13.7 (5,900)
Thermal Conductivity		W/m·K (Btu·in/hr·ft^2·°F)	0.24 (1.65)
Limiting Oxygen Index (LOI)	D2863	%	30-32
Heat Deflection Temperature	D648	°C (°F)	
455 kPa (66 psi)			81 (177)
1620 kPa (264 psi)			51 (123)
Continuous Service Temperature		°C (°F)	150 (302)

*Actual value depends on grade, test specimen, and test conditions.
**Failure defined as stress at 5% strain.

Figure 63 - Typical Properties of ETFE [27]

Physical Properties	Test Condition		ASTM	Typical Values
Thickness				.125"
Specific Gravity			D792	1.80
Rockwell Hardness (M Scale)			D785	100
Moisture Absorption (maximum)			D229	.15%
Flexural Strength	Condition A:	Lengthwise	D229	55,000 psi
		Crosswise		45,000 psi
Tensile Strength	Condition A:	Lengthwise		40,000 psi
		Crosswise		35,000 psi
Compressive Strength	Condition A:	Flatwise	D695	68,000 psi
		Edgewise		35,000 psi
Izod Impact Strength (.500" thick)	E48/50:	Lengthwise	D229	9.5 ft-lb/in.(notch)
		Crosswise		7.5 ft-lb/in.(notch)
Bond Strength (.500" thick)	Condition A		D229	2200 lbs

Thermal & Electrical Properties

Temperature Index Electrical / Mechanical			170° C / 180° C
Coefficient of Thermal Expansion			9.0 cm/cm/°C x 10^{-5}
U.L.® 94 Flammability Rating			94-HB
Dielectric Breakdown (step x step)	Condition A / D 48/50	D229	45.0 kV / 40.0 kV
Maximum Permittivity @ 1 MHz	Condition A / D 24/23	D229	5.20 / 5.40
Maximum Dissipation @ 1 MHz	Condition A / D 24/23	D229	.025 / .035
Electrical Strength (short time)	Condition A	D229	550 Vpm
Electrical Strength (step x step)	Condition A	D229	350 Vpm
Arc Resistance	Condition A	D 495	120 seconds

Figure 64 - Typical Properties of G11 Sheet [40]

	Test Method:			Conditioning	
Mechanical Properties	**EN 61212-2**	**Standard**	**Test Specimen**	**IEC 212**	**Values**
Flexural Strength	4.1	ISO 178	id>100 mm	1	350 Mpa
Compressive Strength, Axial	4.2	ISO 604		1	250 MPa
Tensile Strength, Axial		ISO527			280 MPa
Cohesion between layers	4.3	EN 61212-2	id<100 mm	1	480 MPa
Electrical Properties					
Electric Strength in oil @ 90C:					
Perpendicular to Laminations	5.1	IEC 243-1	3 mm wall thk	2	11.0 kV/mm
Parallel to Laminations	5.1	IEC 243-1	>3 mm wall thk	2	60 kV/25 mm
Insulation resistance after immersion in water	5.2	IEC 167	id>8mm and or od>10mm	4	10,000 M ohm
Permittivity: 50Hz	5.3	IEC 250		3	4.5
1 MHz	5.3	IEC 250		3	4.5
Dissipation Factor: 50Hz	5.3	IEC 250		3	0.01
1 MHz	5.3	IEC 250		3	0.01
Physical and Thermal Properties					
Thermal endurance index @ 20,000 hrs	6.0	IEC 216		-	180°C T.I.
Density	7.2	IEC 1183-A	All	1	1.8 g/cm^3
Water Absorption (maximum)		ASTM D229		4	0.15%

Conditioning: 1: 24h @ 23°C & 50%RH
2: 24h @ 23°C & 50%RH + 1hr in oil at 90°C
3: 96h @ 105°C + 1hr @ 23°C & 20%RH
4: 24h @ 50°C + 24hr in water at 23°C

Figure 65 - Typical Properties of G11 Tube [39]

KYOCERA

FRIALIT F99,7

2021.06.29

Material Type: Aluminium oxide (α-Al_2O_3)

MECHANICAL & PHYSICAL CHARACTERISTICS (TYP.)

Purity		[wt.-%]	>99.5
Density		[g/cm³]	≥3.90
Open porosity		[vol.-%]	0
Average size of crystallites		[µm]	10
Bending strength σ_m DIN EN 843-1		[MPa]	350
Webulls modulus		[-]	>10
Toughness K_{Ic} SEVNB		[MPa*m$^{0.5}$]	3.5
Compressive strength		[MPa]	3500
Young's modulus (static)		[GPa]	380
Poisson's ratio		[-]	0.22
Hardness HV1		[-]	1760
Maximum service temperature in air		[°C]	1950
Linear coefficient of expansion	**-100 - 20 °C** **20 - 500 °C** **20 - 1000°C**	[10^{-6}/K]	5.5 7.3 8.2
Specific heat 20 °C		[J/(kg*K)]	900
Thermal conductivity	**20 °C** **1000 °C** **1500° C**	[W/(m*K)]	34.9 6.8 5.3
Resistivity	**20 °C** **1000 °C**	[Ω*cm]	10^{15} 10^{7}
Dielectric strength		[kV/mm]	>30
Relative permittivity	**70 MHz** **180 MHz** **30 - 40 GHz**	[-]	10 9.9 9.8
Dielectric loss tangent	**70 MHz** **180 MHz** **30 - 40 GHz**	[*10^{-4}]	270*10^{-4} 150*10^{-4} 20*10^{-4}
Typical colour		[-]	ivory

Figure 66 – Properties of FRIALITE F99.7 Aluminum Oxide

Bibliography

[1] TRIUMF, "Our History - Discover Our Lab," [Online]. Available: https://www.discoverourlab.triumf.ca/history/. [Accessed 15 November 2021.]

[2] TRIUMF, "ARIEL | TRIUMF: Canada's particle accelerator centre," TRIUMF,. [Online]. Available: https://www.triumf.ca/ariel. [Accessed 15 November 2021].

[3] J. Pinson, "The power of attraction: magnets in particle accelerators," FermiLab, 19 March 2020. [Online]. Available: https://news.fnal.gov/2020/03/the-power-of-attraction-the-use-of-magnets-in-particle-accelerators/. [Accessed 15 November 2021].

[4] J. E. Milburn, J. T. Tanabe, T. R. Renner, and W. T. Chu, "Raster scanning magnets for relativistic heavy ions," Proc. 1987 IEEE Particle Accelerator Conference: Accelerator Engineering and Technology, Washington, D.C., Mar. 1987, pp. 2000-2002.

[5] C. Yan, N. Sinkinne, and R. Wokcik, "Linear beam raster for cryogenic targets," Elsevier, Nuclear Instruments and Methods in Physics Research A 539, pp. 1–15, 2005.

[6] H. D. Thomsen and S. P. Moller, "Technical Data Package for the ESS Critical Design Review of the Raster Scanning Magnet System," Department of Physics and Astronomy, Aarhus University, Aarhus C, Denmark, Sep. 2015.

[7] "Raster - Hall A Wiki," Thomas Jefferson National Accelerator Facility. [Online]. Available: https://hallaweb.jlab.org/wiki/index.php/Raster. [Accessed 15 November 2021].

[8] M. Alviar-Agnew and H. Agnew, “4.4 The Properties of Protons, Neutrons, and Electrons,” LibreTexts, 03 May 2019. [Online]. Available: https:/chem.libretexts.org/Courses/University_of_British_Columbia/CHEM_100%3A_Foundations_of_Chemistry/04%3A_Atoms_and_Elements/4.4%3A_The_Properties_of_Protons_Neutrons_and_ Electrons. [Accessed 20 December 2021].

[9] A. Gottberg, “ARIEL Electron Driver Beam and Diagnostic Requirements,” TRIUMF, Requirements Specification, Vancouver, BC, Jun. 11 2018.

[10] “Fourier Series,” Brilliant.org. [Online]. Available: https://brilliant.org/wiki/fourier-series. [Accessed 12 April 2022].

[11] “Litz Wire Calculator & Design from YDK Litz Wire & Cabling,” YDK Group. [Online]. Available: https://www.hflitzwire.com/litz-wire-calculation-and-design/. [Accessed 14 March 2022].

[12] Wilson, E., Hozer, B.J., " Beam Dynamics. In: Myers, S., Schopper, H. (eds) Particle Physics Reference Library," CERN (European Organization for Nuclear Research), Geneva, Switzerland, pp 15-18 May. 2020.

[13] Livingood, John J., "Principles of Cyclic Particle Accelerators," D. Van Nostrand, Argonne National Laboratory, Illinois, USA, pp 55-60, 1961

[14] "Table of Resistivity and Conductivity," Thoughtco.com. [Online]. Available: https://www.thoughtco.com/table-of-electrical-resistivity-conductivity-608499. [Accessed 14 May 2022].

[15] "Electrical Resistivity Table for Common Materials," electronics-notes.com. [Online]. Available: https://www.electronics-notes.com/articles/basic_concepts/resistance/electrical-resistivity-table-materials.php. [Accessed 14 May 2022].

[16] "Magnet Circuit," Britannica. [Online]. Available: https://www.britannica.com/science/magnetic-circuit#ref235761. [Accessed 4 April 2022].

[17] "What are Eddy Currents?," Magcraft: Advanced Magnetic Materials. [Online]. Availavle: https://www.magcraft.com/blog/what-are-eddy-currents. [Accessed Mar 14 2022].

[18] "Lenz's Law," Britannica. [Online]. Available: https://www.britannica.com/science/Lenzs-law. [Accessed 4 April 2022].

[19] "Depth of Penetration and Current Density," Iowa State University Center for Nondestructive Evaluation. [Online]. Available: https://www.nde-ed.org/Physics/Electricity/depthcurrentdensity.xhtml. [Accessed 4 April 2022]

[20] Middleton, Wendy M., Van Valkenburg, Mac E., "6-Fundamantals of Networks, Reference Data for Engineers (Ninth Edition)," Newnes, pp 6-1-6-22, 2002.

[21] Planche, T., "Conventional Accelerator Magnet Design," TRIUMF TRI-BN-20-01, Vancouver BC, pp 1-8, 2021.

[22] "Litz Wire, HF-Litz, High Frequency Litz Wire for High Efficiency|ELEKTRISOLA," Elektrisola, [Online]. Available: https://www.elektrisola.com/en/Litz-Wire/Info#design-and-calculation. [Accessed 5 October 2021]

[23] Sullivan, C.R.,"Optimal Choice for Number of Strands in a Litz-Wire Transformer Winding," IEEE Transactions on Power Electronics, vol. 14, no 2, Princton NJ, pp 283-291, 1999.

[24] Zhang, Richard Y., White, Jacob K., Kassakian, John G., "Realistic Litz Wire Characterization using Fast Numerical Simulations," Massachusetts Institute of Technology, Cambridge, MA

[25] “Product Selection Guide,” New England Wire Technologies,” [Online]. Available: https://www.iewc.com/userfiles/documents/products/ne/wt/ca/ta/lo/g/newtcatalog.pdf. [Accessed 5 May 2022].

[26] “Why Preformed Litz Wire Is Your Best Choice for High Current (kHz range) Magnetic Devices,” New England Wire Technologies, [Online]. Available: https://www.newenglandwire.com/why-preformed-litz-wire-is-best-for-high-current-magnetic-devices/. [Accessed 5 May 2022]

[27] “Tefzel ETFE Fluoropolymer Resins Properties Handbook,” Chemours, [Online]. Available: https://www.chemours.com/es/-/media/files/teflon/tefzel-properties-handbook.pdf. [Accessed 3 May 2022].

[28] Sullivan, Charles R., “Simplified Design Method for Litz Wire,” Thayer School of Engineeing at Dartmouth, Hanover, NH, March 2014, pp 2667-2674.

[29] “Coil Winding Wire – MWS Wire – Magnet Wire, Specialty Wire,” MWS Wire Industries, [Online]. Available: https://mwswire.com/magnet-wire/coil-winding-wire/. [Accessed 15 May 2022].

[30] Beynel, P., Maier, P., Schonbacjer, H., “Compilation of Radiation Damage Test Data,” CERN, Geneva, CH, November 1982 pp 31.

[31] “Understanding Phenolic Sheet Benefits and Applications”, Piedmont Plastics, [Online], Available: https://www.piedmontplastics.com/blog/phenolic-sheet-explained. [Accessed 25 May 2022].

[32] Marchetto, M., “Magnetic Field Study for a New Generation High Resolution Mass Spectrometer,” University of British Columbia, Vancouver BC, CA, December 2017 pp 1-123.

[33] “What Is a Magnet Core?,” About Mechanics, [Online]. Available: https://www.aboutmechanics.com/what-is-a-magnetic-core.htm. [Accessed 28 May 2022].

[34] “Ferromagnetic Materials,” Iowa State University Center for Nondestructive Evaluation. [Online]. Available: https://www.ndeed.org/Physics/Magnetism/ferromagmaterials.xhtml. [Accessed 29 May 2022].

[35] “Permeability,” European Passive Components Instutute, [Online]. Available: https://epci.eu/inductors-permeability/. [Accessed 29 May 2022].

[36] “Ferrite,” Britannica. [Online]. https://www.britannica.com/science/ferrite-iron-oxide-compound. [Accessed 30 May 2022].

[37] “J Material,” Magnetics – Ferrite Core Manufacturer, [Online]. Available: https://www.mag-inc.com/Products/Ferrite-Cores/J-Material. [Accessed 20 October 2021].

[38] Russenschuck, S., “Electromagnegt Design of Accelerator Magnets,” CERN, Geneva, CH, pp 441-438.

[39] “Lamitex G11 tube Metric Data rev d,” Franklinn Fibre, [Online]. Available: https://assets-global.website-files.com/5e1cb1ce753a25f3643fb0a7 /5e86413a16db54389eaf183b_Lamitex%2BG11%2Btube%2BMetric%2BData.pdf. [Accessed 2 June 2022].

[40] “Lamitex G11 sheet,” Franklinn Fibre, [Online]. Available: https://assets-global.websitefiles.com/5e1cb1ce753a25f3643fb0a7/5e862a31fe9213a825234b94_Lamitex_G-11_sheet.pdf. [Accessed 2 June 2022].

[41] “Aluminum oxide F99.7,” Kyocera Fineceramic Solutions GmbH, [Online]. Available: https://kyocera-solutions.de/en/materials/f99-7. [Accessed 5 June 2022].

[42] Y.-N. Rao, R. Baartman, “TRI-DN-13-13: Beam Line 4 North (BL4N) Optics Design,” TRIUMF, Requirements Specification, Vancouver, BC, October. 23 2020.